J. Fluid Mech. (1983), *vol.* 127, *pp.* 219–261
Printed in Great Britain

The structure of a separating turbulent boundary layer. Part 4. Effects of periodic free-stream unsteadiness

By ROGER L. SIMPSON, B. G. SHIVAPRASAD AND Y.-T. CHEW†
Department of Civil and Mechanical Engineering, Southern Methodist University, Dallas, Texas 75275

(Received 17 February 1982)

Unsteady separating turbulent boundary layers are of practical interest because of unsteady aerodynamic phenomena associated with blades in compressors and with helicopter rotors in translating motion during high-loading conditions. Extensive measurements of a steady free-stream, nominally two-dimensional, separating turbulent boundary layer have been reported by Simpson, Chew & Shivaprasad (1981*a*, *b*) and Shiloh, Shivaprasad & Simpson (1981). Here measurements are reported that show the effects of sinusoidal unsteadiness of the free-stream velocity on this separating turbulent boundary layer at a practical reduced frequency of 0·61. The ratio of oscillation amplitude to mean velocity is about 0·3.

Upstream of flow detachment, single- and cross-wire, hot-wire anemometer measurements were obtained. A surface hot-wire anemometer was used to measure the phase-averaged skin friction. Measurements in the detached-flow zone of phase-averaged velocities and turbulence quantities were obtained with a directionally sensitive laser anemometer. The fraction of time that the flow moves downstream was measured by the LDV and by a thermal flow-direction probe.

Upstream of any flow reversal or backflow, the flow behaves in a quasisteady manner, i.e. the phase-averaged flow is described by the steady free-stream flow structure. The semilogarithmic law-of-the-wall velocity profile applies at each phase of the cycle. The Perry & Schofield (1973) velocity-profile correlations fit the mean and ensemble-averaged velocity profiles near detachment.

After the beginning of detachment, large amplitude and phase variations develop through the flow. Unsteady effects produce hysteresis in relationships between flow parameters. As the free-stream velocity during a cycle begins to increase, the Reynolds shearing stresses increase, the detached shear layer decreases in thickness, and the fraction of time $\hat{\gamma}_{pu}$ that the flow moves downstream increases as backflow fluid is washed downstream. As the free-stream velocity nears the maximum value in a cycle, the increasingly adverse pressure gradient causes progressively greater near-wall backflow at downstream locations, while $\hat{\gamma}_{pu}$ remains high at the upstream part of the detached flow. After the free-stream velocity begins to decelerate, the detached shear layer grows in thickness and the location where flow reversal begins moves upstream. This cycle is repeated as the free-stream velocity again increases.

† Present address: Department of Mechanical and Production Engineering, University of Singapore.

1. Introduction

1.1. *Importance of unsteady turbulent boundary layers*

Unsteady turbulent boundary layers have become the subject of much recent interest because of unsteady aerodynamic phenomena associated with blades in compressors and with helicopter rotors in translating motion. While all turbulent flows are inherently unsteady, the term 'unsteady' will mean here a periodic time-dependent motion, in contrast with the relatively aperiodic motion of turbulence. The boundary layers cannot be ignored in unsteady-flow analyses of these devices because there is considerable interaction between the boundary layer and the inviscid flow during high-loading conditions. In such cases the relatively thick boundary layer on the suction side of the lifting body is near separation. 'Separation' must mean the entire process of 'departure' or 'breakaway' or the breakdown of the boundary-layer concept. An abrupt thickening of the rotational-flow region next to a wall and significant values of the normal-to-wall velocity component must accompany breakaway, or else this region will not have any significant interaction with the free-stream inviscid flow (Simpson 1981). 'Detachment' is the locus of points where the limiting streamlines of the flow leave the surface.

In spite of its importance, relatively little fundamental work has been done toward describing the behaviour of unsteady turbulent shear flows near separation and downstream. Simpson, Chew & Shivaprasad (1981*a*, *b*) and Shiloh, Shivaprasad & Simpson (1981) have reported extensive measurements of a steady free-stream separating turbulent boundary layer produced on the floor of the wind-tunnel test section shown in figure 1. The Reynolds number for that flow was $4{\cdot}7 \times 10^6$, based on the entrance free-stream velocity $\overline{U}_{ei}$ of 15·06 m/s and the 4·9 m length C of the converging–diverging section. This paper reports the effects of sinusoidal unsteadiness of the free-stream velocity on this separating turbulent boundary layer at a practical reduced frequency $k = \omega C/2\overline{U}_{ei}$ of 0·61. The ratio of oscillation amplitude to mean velocity is about 0·3.

As background for this paper, a brief summary is given of the steady free-stream separating boundary layer so that the effects of periodic free-stream unsteadiness can be distinguished. In addition, a description of unsteady turbulent-flow terminology is given, and a brief review of some key earlier results and concepts are discussed.

1.2. *The nature of a steady free-stream separating turbulent boundary layer*

For steady free-stream mean-two-dimensional separating turbulent boundary layers, a set of quantitative definitions on the detachment state near the wall has been proposed (Simpson 1981): *incipient detachment* (ID) occurs with instantaneous backflow 1% of the time; *intermittent transitory detachment* (ITD) occurs with instantaneous backflow 20% of the time; *transitory detachment* (TD) occurs with instantaneous backflow 50% of the time; and *detachment* (D) occurs where the time-averaged wall shearing stress $\bar{\tau}_w = 0$. Thus the fraction of time with forward flow γ_{pu} is a descriptive parameter for identifying these stages and should be documented in all separated-flow experiments.

Figure 1 shows a qualitative sketch of the steady free-stream bottom-wall turbulent shear flow studied with a laser anemometer at SMU and the locations of ID, ITD and D when determined 1 mm from the wall. The mean flow upstream of ID obeys the 'law of the wall' and the 'law of the wake' as long as the maximum shearing stress $-\rho\overline{uv}_{max}$ is less than $1{\cdot}5\tau_w$. The qualitative turbulence structure is not markedly different from the zero-pressure-gradient case. The 'bursting' frequency

FIGURE 1. Sideview schematic diagram of the test section with the steady free-stream separating turbulent boundary layer (Simpson *et al.* 1981*a*) on the bottom wall. The major divisions on the scales are 10 in. Note the baffle plate upstream from the blunt leading edge on the bottom test wall and side- and upper-wall jet boundary-layer controls.

n of the most-energetic eddies near the wall is correlated by $U_e/n\delta = 10$, where U_e is the mean velocity outside the boundary layer and δ is the boundary-layer thickness.

When $-\rho\overline{uv}_{max} > 1{\cdot}5\tau_w$, the Perry & Schofield (1973) mean-velocity-profile correlation and the law of the wall apply upstream of ITD. Up to one-third of the turbulence energy production in the outer region is due to normal-stress effects, which modify the relations between dissipation rate, turbulence energy and turbulent shearing stress that are observed farther upstream. The spanwise integral lengthscale of the turbulence increases with δ^2, and the bursting frequency n continues to be about equal to $U_e/10\delta$. Pressure-gradient relaxation begins near ITD and continues until D.

Downstream of detachment, the mean backflow profile scales on the maximum negative mean velocity U_N and its distance N from the wall. A U^+ *vs.* y^+ law of the wall is not consistent with this result since U_N and N increase with streamwise distance while $\nu(\tau/\rho)_w^{\frac{1}{2}}$ varies with $(\tau/\rho)_w^{\frac{1}{2}}$. High turbulence levels exist in the backflow, with u- and v-fluctuations of the same order as $|U|$. $-\overline{uv}/u'v'$ becomes lower with increasing backflow, and is about 25% lower in the outer region than for the upstream attached flow. Mixing-length and eddy-viscosity models are adequate upstream of detachment and in the outer region, but are physically meaningless in the backflow. γ_{pu} never reaches zero, indicating that there is no location with backflow all of the time. Normal and shear stresses turbulence energy production in the outer region supply turbulence energy to the backflow by turbulence diffusion where it is dissipated. Negligible turbulence-energy production occurs in the backflow.

This turbulence-energy diffusion and the small mean backflow are supplied intermittently by large-scale structures as they pass through the detached flow as suggested by figure 1. The backflow does not come from far downstream. The frequency of passage n of these large-scale structures also varies as U_e/δ and is about an order of magnitude smaller than the frequency far upstream of detachment. Reynolds shearing stresses in the backflow must be modelled by relating them to the turbulence structure and not to local mean-velocity gradients. The mean-velocity profiles in the backflow are a result of time-averaging of the large fluctuations and are not related to the cause of the turbulence.

1.3. *Some background on unsteady turbulent boundary layers*

For periodic unsteady turbulent flow, the ensemble average $\hat{F}$ of instantaneous values of a quantity $\mathscr{F}$ for a specific phase $2\pi t/T$ of the outer-flow oscillation is given by

$$\hat{F} = \lim_{N\to\infty} \frac{1}{N} \sum_{n=1}^{N} \mathscr{F}(t+nT), \tag{1.1}$$

where T is the period of the imposed oscillation and N is the number of cycles that are averaged. This ensemble average is also called a 'periodic sample' or a 'phase average'. $\mathscr{F}$ can also be represented as

$$\mathscr{F} = \overline{F} + \tilde{F} + f, \tag{1.2}$$

where $\overline{F}$ is the time-averaged or mean value, $\tilde{F}$ is the periodic oscillation and f is the turbulent fluctuation. By comparison of these two equations

$$\hat{F} = \overline{F} + \tilde{F}. \tag{1.3}$$

The ensemble-averaged variance for the turbulent fluctuation is given by

$$\hat{f^2} = \lim_{N\to\infty} \frac{1}{N} \sum_{n=1}^{N} (\mathscr{F} - \hat{F})^2, \tag{1.4}$$

$$\hat{f^2} = \overline{f^2} + \tilde{f^2}, \tag{1.5}$$

where $\overline{f^2}$ is the time-averaged or mean value and $\tilde{f^2}$ is the periodic oscillation of the variance. The periodic oscillations $\tilde{F}$ and $\tilde{f^2}$ are presented here in terms of their Fourier components

$$\tilde{F} = \sum_{n=1}^{\infty} \tilde{F}_n \cos(n\omega t - \phi_n), \tag{1.6}$$

$$\tilde{f^2} = \sum_{n=1}^{\infty} \tilde{f}_n^2 \cos(n\omega t - \lambda_n). \tag{1.7}$$

Note the sign convention used for the phase angles ϕ_n and λ_n.

Unsteady turbulent boundary layers are governed by the same equations as for the steady case, except that time-dependent effects must be included. The continuity and streamwise momentum equations for incompressible unsteady turbulent boundary layers are respectively

$$\frac{\partial \hat{U}}{\partial x} + \frac{\partial \hat{V}}{\partial y} = 0, \tag{1.8}$$

$$\frac{\partial \hat{U}}{\partial t} + \hat{U}\frac{\partial \hat{U}}{\partial x} + \hat{V}\frac{\partial \hat{U}}{\partial y} = \frac{\partial \hat{U}_e}{\partial t} + \hat{U}_e\frac{\partial \hat{U}_e}{\partial x} + \frac{\partial}{\partial y}\left[\nu\frac{\partial \hat{U}}{\partial y} - \widehat{uv}\right]. \tag{1.9}$$

Here $\hat{U}$ and $\hat{V}$ are ensemble-averaged streamwise and normal-to-wall velocity components and $-\widehat{uv}$ is the ensemble-averaged Reynolds shear stress.

The difficulty of solving these equations is the same as that for steady flows, namely describing the behaviour of $-\widehat{uv}$. A number of investigators have argued that, as long as the period of the organized unsteadiness is relatively long compared with the turbulence timescales, it should be acceptable to use the approximation that the turbulence structure is unaffected by the unsteadiness. Quasi-steady flow exists when the phase-averaged flow can be described by the steady free-stream flow structure. When the frequency of the organized unsteadiness is comparable to energy-containing turbulence frequencies, this approximation cannot be used. Substantial interaction

between the organized and unorganized time-dependent motions would be expected. For example, Acharya & Reynolds (1975) have shown that several turbulence models fail for the latter condition in an unseparated channel flow.

Bradshaw (1978) pointed out that the substantial derivative of $-\widehat{uv}$, $D(-\widehat{uv})/Dt$, for the ensemble-averaged movement of a fluid element cannot exceed values for which the turbulence model is satisfactory in steady flow and still be valid in unsteady flow. Separate bounds on the streamwise wavelength and on frequency in a spatially dependent unsteady flow are not required; the upper limit on the frequency seen by a moving fluid element can be derived from steady-flow considerations. If a steady-flow turbulence model cannot respond to spatial changes with a wavelength less than L, then the moving-axis frequency of the unsteady flow cannot exceed $\bar{U}_e/L$.

Nearly all of the experimental data that have been obtained have been outside the viscous sublayer and near-wall region. Patel (1977) measured $\hat{U}$ and $\widehat{u^2}$ in travelling-wave zero-mean-pressure-gradient flows for oscillation amplitudes up to 11 % of the mean free-stream velocity and frequencies of 4–12 Hz. Kenison (1977) obtained the same type of measurements and Preston-tube skin-friction results in the same tunnel with a mean adverse pressure gradient. The O.N.E.R.A. group (Houdeville, Desopper & Cousteix 1976; Cousteix, Desopper & Houdeville 1977; Cousteix, Houdeville & Raynaud 1979) have obtained $\hat{U}$, $\widehat{u^2}$, $-\widehat{uv}$, $\widehat{v^2}$ and kurtosis measurements for zero-mean-pressure-gradient and adverse-pressure-gradient time-dependent flows. The oscillation frequency was between 38 and 43 Hz with the oscillation amplitudes of 0·1–0·37 of the mean free-stream velocity. All of these measurements indicate that outside the near-wall region the turbulence structure is basically unaffected by organized unsteadiness.

Davis (1974) used a dynamical model to predict perturbation turbulent Reynolds stresses outside of the viscous sublayer. He assumed that an infinitesimal perturbation results in a linear change in the statistics of the turbulence and that the turbulence is either weak or that the turbulent perturbations are quasi-Gaussian. He applied this to long-wave perturbations, finding that the perturbation shear stress is of primary dynamical importance and is determined by the spectrum of $\overline{v^2}$ and the perturbation velocity $\tilde{U}$. Large shear values for a given spectral frequency occur at its critical height. After summing this interaction between the periodic and all turbulent motions, he obtained the result

$$\tilde{\tau} = 2K(-\overline{uv})^{\frac{1}{2}} y \frac{d\tilde{U}}{dy} \tag{1.10}$$

for the perturbation shear stress outside the viscous sublayer, where K is the von Kármán constant.

In their unseparated channel flow, Acharya & Reynolds (1975) measured a substantial phase lead for the sublayer oscillation over the core-flow velocity in their 24 Hz experiment. A substantial phase lag was observed in the sublayer for a frequency of 40 Hz, which was the bursting frequency for the steady flow with the same mean velocity. Karlsson (1959) also reported a phase shift of as much as 35° in the viscous sublayer, but he did not have enough data to isolate the effect. Here measurements in the viscous sublayer and a simple analysis indicate that phase shifts in the viscous sublayer can be due to small probe and test-wall oscillations at the periodic frequency.

In view of the previous research, it was expected that most of the phenomena of interest in practical flows could be handled by steady turbulence models, although

an insufficient data base was available to confirm this assumption. Consequently, it was somewhat surprising to find substantial unsteadiness effects in the separating and separated-flow region. Results from laser and hot-wire anemometer measurements in the separating flow region are presented here.

2. Experimental equipment

2.1. *Wind tunnel*

The mainstream flow of the blown open-circuit wind tunnel is introduced into the test section after first passing through a filter, blower, a fixed-setting damper, the rotating-blade damper discussed in §2.2, a section of honeycomb to remove the mean swirl of the flow, seven screens to remove much of the turbulence intensity, and finally through a two-dimensional 4:1 contraction-ratio nozzle to further reduce the longitudinal turbulence intensity while accelerating the flow to test speed.

Figure 1 is a side-view schematic of the 8 m long, 0·91 m wide test section of the wind tunnel. The upper wall is adjustable such that the free-stream velocity or pressure gradient can be adjusted. The sidewalls are made of float plate glass to prevent laser signal dispersion, while the upper wall is made of Plexiglas.

The test wall is constructed from 18 mm thick fin-form plywood, reinforced every 28 cm with $7{\cdot}6 \times 3{\cdot}8 \times 0{\cdot}6$ cm cross-section steel channel. This reinforcement was necessary since Acharya & Reynolds (1975) found that test-wall vibration amplitudes as small as 0·025 mm produced up to a 10 % error in $\tilde{U}$-measurements near the wall. They reduced their vibrations by adding a large amount of mass to the test wall. In the present case, the entire weight of the test section rests on the test wall and the steel reinforcements. Nevertheless, some test-wall oscillation was still present in the experiments reported here, as discussed in §4.

The active boundary-layer control system, which is described by Simpson, Chew & Shivaprasad (1980*a*), was installed on the non-test walls of the test section to inhibit undesirable flow three-dimensionality and to prevent separation. Because the static pressure in the test section is time-varying in unsteady experiments, no passive boundary-layer control can be used that depends on a steady test section pressure higher than the pressure outside the tunnel. Highly two-dimensional wall jets of high-velocity air are introduced at the beginning of each of the eight-feet long sections. At the latter two streamwise locations the oncoming boundary layer is partially removed by a highly two-dimensional suction system. The flows in this control system are relatively insensitive to the ± 1 cm of water static-pressure oscillations in the test section. The large volume of the control system and the 30 cm of water static pressure loss in its components act as a large low-pass frequency filter. Dynamic-pressure oscillations of the wall jet flow were of the order $\pm 0{\cdot}04$ cm of water.

The inviscid core flow is uniform within 0·05 % in the spanwise direction and within 1 % in the vertical direction. The test-wall boundary layer is tripped by the blunt leading edge of the plywood floor, the height of the step from the wind-tunnel contraction to the test wall being 0·63 cm. Smoke can be introduced uniformly into the boundary layer just upstream of this trip for use with the laser anemometer.

2.2. *Programmable-rotating-blade damper*

Investigators of unsteady flows normally have little control over the waveform of the flow unsteadiness. Although the waveform may consist principally of a given frequency, substantial contributions normally come from higher harmonics. In anticipation of nonlinear effects produced within an unsteady turbulent boundary

layer, a programmable-rotating-blade damper and control system were designed, constructed and used to produce a nearly single harmonic sinusoidal waveform without wind tunnel resonance. This feature allows one to attribute any large higher-harmonic effects within the boundary layer to boundary-layer processes, rather than to combined effects with inviscid flow higher harmonics of the free stream.

Simpson, Sallas & Nasburg (1978) describe this rotating-blade-damper feedback control system in more detail. In essence, the angular velocity of the rotating blades in the damper is varied during a cycle so as to produce the desired waveform shape, amplitude, and frequency. In the current experiment, the 0·596 Hz oscillation had a velocity amplitude that was about 0·3 mean velocity. In these cases the amplitudes of the second and third harmonics were about 2–3 % of the first harmonic. For comparison, it should be noted that for constant-angular-velocity blade rotation the amplitude of the second harmonic is 14 % of the first harmonic.

All events during an oscillation cycle were synchronized with respect to a 'reference' square-wave voltage signal at the oscillation frequency that is generated by the quartz clock in the control electronics. A 'clock' square-wave voltage signal with a frequency 96 times the reference signal is also generated to aid data acquisition. Data were acquired at the beginning of each of these 96 bins of an oscillation cycle.

The variation in the period of each flow cycle, or the 'jitter', follows a Gaussian distribution with a standard deviation of 0·15 %. This indicates a high degree of repeatability from cycle to cycle. As pointed out in appendix A this jitter has no effect on ensemble-averaged velocity values and only a very small effect on turbulent-fluctuation measurements. Results obtained several weeks apart indicate long-term stability of the electronic system and long-term repeatability, which are important when performing experiments over a period of months.

2.3. *Hot-wire anemometers and surface hot-wire skin-friction element*

Miller (1976)-type integrated circuit hot-wire anemometers and linearizers, as modified by Simpson, Heizer & Nasburg (1979) were constructed and used here and by Simpson *et al.* (1981*a*). The frequency response was flat up to 7·5 kHz for an overheat ratio of 0·7. This moderately high overheat ratio was used for two reasons. First, as shown by Wood (1975) the range of flat frequency response is improved with a higher overheat ratio. Secondly, a 0·2 °C wind-tunnel air-temperature oscillation amplitude was present at the flow oscillation frequency due to periodic dissipation and compressibility effects. In order to make this air-temperature oscillation have a negligible effect on the hot-wire behaviour, an overheat ratio as high as safely possible was desired. In the present case this oscillation amplitude was only 0·04 % of the temperature difference between the wire and the air, so no corrections to hot-wire measurements were made for this effect.

Standard TSI model 1274-T1.5 normal wire and model 1248-T1.5 cross-wire probes were used for boundary-layer measurements. The closest to the wall that these probes could safely make measurements was about 0·05 mm and 0·9 mm respectively. The detailed streamwise free-stream velocity distributions were obtained using the Model 1274-T1.5 probe mounted on a mobile cart.

A standard TSI model 1015 C correlator was used to obtain sum and difference values for u and v from cross-wire signals. When using the electronic multipliers to determine the ensemble-averaged turbulence quantities $-\widehat{uv}$, $\widehat{u^2v}$, and $\widehat{v^3}$, each linearized hot-wire signal was passed first through a $Q = 5$ band-reject filter (Burr–Brown UAF41 Universal Filter) that was adjusted for 40 dB attenuation at

0·596 Hz and for only 3 dB attenuation at $\pm 10\%$ on either side of this frequency. This eliminated the organized periodic fluctuation from the signals.

The traversing mechanism used for the boundary-layer velocity measurements was mounted on the supporting frame for the upper wall and provided for precise positioning of the probe sensors. A cathetometer was used to accurately locate the probe sensor from the wall within an uncertainty of about $\pm 0{\cdot}05$ mm.

A TSI Model 1050 anemometer was used with the Rubesin-type surface hot-wire-skin-friction element that is described by Simpson *et al.* (1981*a*). Results obtained for the steady free-stream flow by these workers agreed with the Ludwieg–Tillman (1950) skin friction equation within the experimental uncertainties.

2.4. *Laser anemometer*

The laser anemometer used in these experiments is described in some detail by Simpson & Chew (1979). In essence this is a two-velocity-component (U, V) directionally sensitive fringe-type system that has been used in earlier work (Simpson, Strickland & Barr 1977; Simpson *et al.* 1981*a*). The unshifted and 25 MHz Bragg-cell shifted beams lie in an almost horizontal plane and measure the streamwise velocity with vertical fringes. The unshifted and 15 MHz Bragg-cell shifted beams lie in a vertical plane and measure $(\mathscr{V} \cos 4{\cdot}4° + \mathscr{W} \sin 4{\cdot}4°)$ with almost-horizontal fringes. The 25 MHz and 15 MHz beams form a third fringe pattern that measures $(\mathscr{U} - \mathscr{V} \cos 4{\cdot}4° - \mathscr{W} \sin 4{\cdot}4°)/\sqrt{2}$ around 10 MHz. Since

$$\widehat{u^2} \quad \text{and} \quad \widehat{(v \cos 4{\cdot}4° + w \sin 4{\cdot}4°)^2}$$

were measured independently and $\widehat{uw}$ was presumed very small, the Reynolds shearing stress $-\widehat{uv}$ resulted from this measurement. Signal processing was by fast-sweep-rate sampling spectrum analysis, as described by Simpson & Barr (1975).

The 1 μm dioctyl phthalate particles follow the highly turbulent oscillations found in separated regions (Simpson & Chew 1979). It should be noted that it is impossible to seed a highly turbulent flow in any prescribed manner. Highly turbulent flows are characterized by intense mixing with the flow. In this case there is also significant entrainment of free-stream fluid into the turbulent motions. This would progressively dilute the particle concentration if only the shear flow has been seeded. Instead of needless worry over prescribed particle concentration, concern has been with proper averaging of available signals as described by Simpson *et al.* (1981*a*), with enough particles to provide a high data rate, and with sufficiently small particles to follow the flow accurately.

The LDV signal was treated the same as a continuous hot-wire signal, even though it is discontinuous. The LDV signal data rate must be sufficiently large that the latest signal-processing output voltage is obtained since the sample for the last bin was taken. This ensures that there is no more than one bin uncertainty in the phase information. Here the minimum required data rate is 58 samples/s, but, since these new signals are not equally spaced in time, a higher data rate is necessary. About 400 new signals per second were obtained, which produced satisfactory $\hat{U}$, $\widehat{u^2}$, $\hat{V}$ and $\widehat{v^2}$ results.

2.5. *Near-wall flow-direction probe*

As mentioned in §1, the fraction of time γ_{pu} that the flow moves in a downstream direction is a descriptive parameter of the near-wall detached flow. Although the LDV is a versatile technique for detailed separated flow measurements, a simpler and less-expensive technique using hot-wire sensors can be used to measure γ_{pu}. Rubesin

et al. (1975) demonstrated that the wake from a heater wire can heat either an upstream or downstream hot-wire sensor to determine the flow direction. Later Eaton *et al.* (1979) developed this 'thermal-tuft' technique and built electronic circuitry for making use of this probe for the measurement of γ_{pu} in separated flows behind a backward-facing step and diffuser. Ashjaee & Johnston (1980) made extensive use of this probe in their transitory stall studies in diffusers. Since the thermal tuft provides continuous signals rather than discrete signals as provided by the LDV, it is suited for measurements in unsteady flow where signal averaging is required for each phase of a flow cycle.

Shivaprasad & Simpson (1982) describe in detail a thermal tuft that was used in these experiments. Like the Eaton *et al.* design, this tuft had 6 mm long parallel heater and sensor wires that were 2·5 mm apart and were oriented perpendicular to the mainstream flow direction. In addition, Shivaprasad & Simpson added one 5 mm long heater on each side of this array and 2·5 mm from the end of the sensors to improve sensitivity to crossflows. Results obtained with this probe are in agreement within $\pm 0{\cdot}06$ uncertainty with direct LDV measurements of γ_{pu} that are $\pm 0{\cdot}07$ uncertain. For values of γ_{pu} not near zero or unity, the thermal tuft produces values that are 0·05 to 0·1 higher than the LDV values.

2.6. *Signal processing*

An EAI 690 Hybrid computer was operated in a real-time data-acquisition mode to determine ensemble-averaged velocities and turbulence fluctuations. The reference and clock square-wave signals from the programmable rotating-blade-damper control system were used to trigger data acquisition. The negative-going slope of the reference signal marked the beginning of an oscillation cycle. The negative-going slope of the clock signal marked the acquisition of data for one of 96 different phases of the fundamental period. The Fortran program determined signal averages and variances for each of these 96 phases for any number of oscillation cycles, which was 200 for all data presented here.

A Princeton Applied Research Model 4512 Fast-Fourier-Transform Spectrum Analyzer was used to determine the harmonic content of the organized periodic motion and the spectral content of the boundary-layer turbulence. In the first application, it was used with the DC to 10 Hz range to verify that no extraneous periodic frequencies existed during an experiment and to aid the rapid initial adjustment of the programmable rotating-blade-damper control system in reducing all but the fundamental harmonic. In the measurement of turbulence spectra with the DC to 2 kHz range, a phase-selector circuit, described below, was used to activate the acquisition of signals only during a selectable phase of the periodic cycle.

A phase-selector circuit was constructed to produce a voltage pulse that activated the FFT only during a desired phase range of a cycle. A Signetics 556 Dual Timer was trimmed such that a voltage pulse, $\frac{1}{8}$ of the reference signal period long, could be selected for one of 16 equally spaced phases of a cycle. For example, with the selector switch in the first position, the centre of the 45° wide pulse was located at 22·5°.

Other electronic equipment included a SAICOR model 41 Digital Correlation and Probability Analyzer, an Applied University Research four-channel FM tape recorder (response down 3 db at 2 kHz), a voltage comparator or Schmitt trigger using an operational amplifier integrated circuit, and signal multipliers using Analog Devices AD533 JH integrated circuits trimmed to within ± 1 % full-scale nonlinearity error. A true integrating voltmeter consisting of a voltage-controlled oscillator (Tektronix

FG501 Function Generator) and a digital counter (Tektronix DC503 Universal Counter) was used in checking the voltage-signal mean values with the computer results.

3. Description of the test flow

The free-stream mean-velocity distribution for this periodic unsteady flow was essentially the same as the steady free-stream flow examined by Simpson *et al.* (1981*a*, *b*). Figures 2 and 3 show the streamwise distributions of several parameters associated with the sinusoidal waveform flow discussed here and the steady free-stream flow. All data were obtained at atmospheric pressure and $25 \pm 0{\cdot}25$ °C conditions.

The ensemble-averaged free-stream velocity $\hat{U}_e$ outside the boundary layer can be expressed in terms of its Fourier components $\tilde{U}_{ne}$ as

$$\hat{U}_e = \overline{U}_e \left\{ 1 + \sum_{n=1}^{\infty} \left[\frac{\tilde{U}_{ne}}{\overline{U}_e} \cos(\omega n t - \phi_{ne}) \right] \right\}. \tag{3.1}$$

Figure 2 shows that the mean free-stream velocity $\overline{U}_e$ obtained along the tunnel centreline using the single-wire probe was repeatable within about 3 % over the duration of these experiments, which is slightly greater than the uncertainty of measuring the mean velocity with a hot-wire anemometer ($\pm 2{\cdot}4$ %). Upstream of 3 m, the first harmonic ratio $\tilde{U}_{1e}/\overline{U}_e$ was about 0·3 and was repeatable within 2 %, while ϕ_{1e} only varied 4°.

Although the variable-angular-velocity rotating-blade damper tended to eliminate higher-harmonic effects, second and third harmonics had amplitudes of about 2 % of the first harmonic. The scatter was about ± 15 % for $\tilde{U}_{2e}/\overline{U}_e$ and only ± 5 % for $\tilde{U}_{3e}/\overline{U}_e$ upstream of detachment. Because of the relatively small contribution by these harmonics, relatively greater scatter in ϕ_{2e} and ϕ_{3e} results, being $\pm 40°$ and $\pm 10°$ respectively. Fast-Fourier signal analysis revealed that only 0·298 Hz, which is the rotating-damper-blade frequency, and higher harmonics produce periodic velocity contributions.

Using this streamwise distribution, the free-stream streamwise pressure gradient can be calculated from the unsteady inviscid equation of motion. The important terms are from the mean and first harmonics and are given by

$$\frac{1}{\rho}\frac{d\hat{P}}{dx} = -[\overline{U}_e\,\overline{U}'_e + \tfrac{1}{2}\tilde{U}_{1e}\,\tilde{U}'_{1e}] + [(\overline{U}_e\,\tilde{U}'_{1e} + \tilde{U}_{1e}\,\overline{U}'_e)^2 + \tilde{U}^2_{1e}(\overline{U}_e\,\phi'_{1e} - \omega)^2]\cos(\omega t - \phi_{1e} - 180° - \gamma_{1e}), \tag{3.2}$$

where

$$\gamma_{1e} = \arctan\left\{ \frac{\tilde{U}_{1e}(\overline{U}_e\,\phi'_{1e} - \omega)}{\overline{U}_e\,\tilde{U}'_{1e} + \tilde{U}_{1e}\,\overline{U}'_e} \right\}. \tag{3.3}$$

Here primes denote a streamwise derivative. These derivatives were evaluated at a given streamwise location by differentiating the least-squares curve fit of a quadratic model to the five data points nearest that location. The first harmonic contributes a term to the mean-pressure gradient because of the quadratic term in the inviscid equation of motion. Here the mean-pressure gradient is about $\frac{12}{18}$ of that due to the mean-velocity term alone upstream of separation.

Figure 3 shows the non-dimensional mean, maximum, and minimum pressure gradients dC_p/dx along the centreline of the test wall. Here $C_p = 2(P - P_i)/\rho\overline{U}^2_{ei}$, where i denotes the nominal free-stream entrance condition with $\overline{U}_{ei} = 15{\cdot}06$ m/s, which is the same as in the steady free-stream case. The mean-pressure gradient

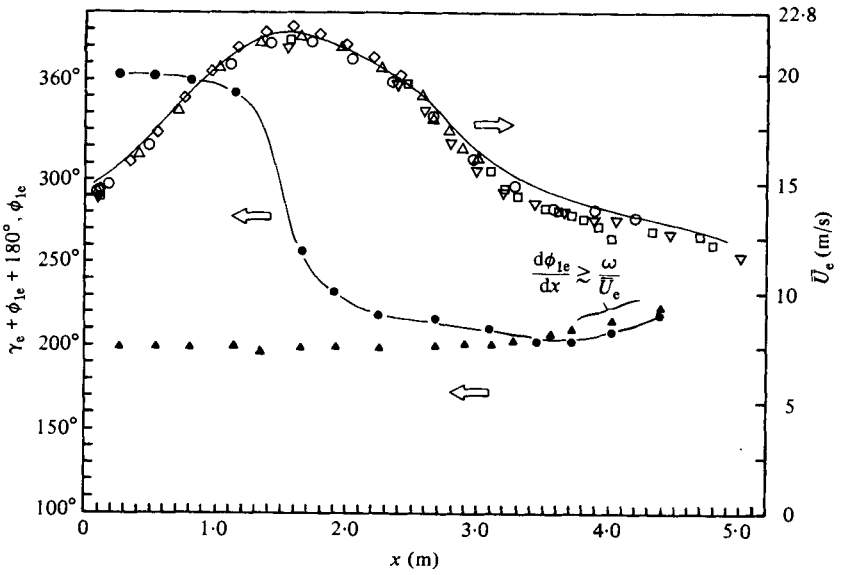

FIGURE 2. Free-stream flow conditions for the steady free-stream flow of Simpson *et al.* (1981*a*) and the present unsteady flow. $\bar{U}_e$: ——, steady flow; open symbols, sinusoidal unsteady flow on different days. Phase angles of first harmonics: ▲, ϕ_{1e}, free-stream velocity; ●, $\phi_{1e}+180°+\gamma_{1e}$, pressure gradient (dashed line for visual aid).

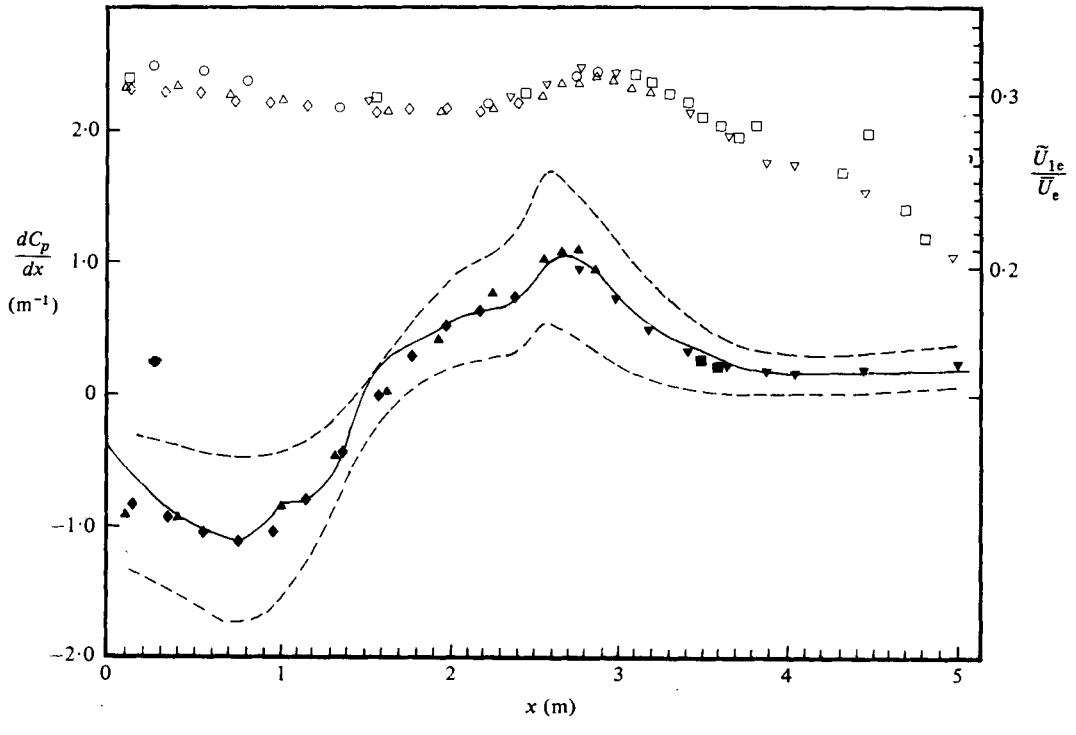

FIGURE 3. Ratio $\bar{U}_{1e}/\bar{U}_e$ of free-stream amplitude to mean-velocity and pressure-gradient distributions along the centreline. $C_p = 2(P-P_1)/\rho\bar{U}_{e1}^2$, $\bar{U}_{ei} = 15{\cdot}06$ m/s. ——, steady flow of Simpson *et al.* (1981*a*); – – –, limits of the unsteady pressure gradient; symbols denote unsteady flow on different days.

closely agrees with the steady free-stream pressure gradient except near the throat at the 1·5 m location. The amplitude of the first-harmonic pressure gradient shown in figure 3 is about 0·55–0·6 of the mean-pressure gradient upstream of detachment and not near the test-section throat. After detachment the pressure gradient relaxes so that $d\hat{P}/dx$ is *never* negative or a favourable pressure gradient. Figure 2 shows ϕ_{1e} and the phase angle of the pressure gradient first harmonic $\phi_{1e} + 180° + \gamma_{1e}$, and shows that the first-harmonic pressure gradient strongly lags the local free-stream velocity in the converging section of the tunnel. The lag is considerably lower in the diverging section. After detachment the oscillatory-pressure gradient only slightly leads the velocity oscillation with the onset of pressure-gradient relaxation.

The mean free-stream streamwise turbulence intensity was less than 1 % upstream of separation and was nearly independent of streamwise position, indicating no strong influence of flow acceleration or deceleration. Fast-Fourier signal analysis showed that, downstream of separation, the increasingly greater free-stream turbulence intensity of up to 2 % contained appreciable contributions at frequencies under 10 Hz. As pointed out in §1, the frequency of passage of large eddies in the separated shear flow is in this range. Since it is well known that the large entraining eddies in a turbulent boundary layer can induce irrotational fluctuations in the adjacent free-stream (Phillips 1955), this is believed to be the main source of these greater free-stream turbulence intensities.

To examine the two-dimensionality of the mean boundary-layer flow, smoke was introduced only in a spanwise portion of the test wall boundary layer at a given time. A sheet of laser light produced by a cylindrical lens was used to illuminate the smoke. Upstream of separation, negligible spanwise diffusion of the smoke was observed, indicating no gross flow three-dimensionality. For the comparable steady free-stream flow shown in figure 2, velocity profiles at several spanwise locations indicated that the mean velocity was two-dimensional within 1 % (Simpson *et al.* 1980*a*, 1981*a*). Downstream of separation greater spanwise diffusion occurred, so that downstream of 4·4 m no nominally two-dimensional flow remained. On the basis of these observations, the wall jet and suction boundary-layer controls were adjusted to the same setting to produce a nearly two-dimensional flow pattern downstream of separation for both the steady and unsteady free-stream flows. Smoke-flow patterns in the sidewall and corner flows were symmetric about the channel centreline for both flows.

The momentum integral equation provides a global test of two-dimensionality based on conservation of momentum over a large flow volume. The summed skin-friction and normal-stress terms and the summed momentum and pressure gradient terms of the integrated form of the momentum integral equation differed no more than 16 % over 80 % of the length of separation of the steady free-stream flow of Simpson *et al.* (1980*a*, 1981*a*). This difference was within the experimental uncertainty due to uncertainties in measured quantities. For the unsteady flow discussed here, the difference between the summed momentum and pressure-gradient terms and the skin-friction term was less than 25 % for the mean flow and for the first harmonic upstream of 3·5 m. The experimental uncertainties of measured quantities produced an uncertainty of ± 30 % in closing the momentum integral balance. Thus the unsteady flow discussed here satisfies the two-dimensional momentum integral equation within experimental uncertainties.

Normal hot wire	$U \pm 2{\cdot}4\,\%$, $\overline{u^2} \pm 7\,\%$
Cross hot wire (including misalignment uncertainty)	$U \pm 3{\cdot}2\,\%$, $\overline{u^2} \pm 10\,\%$ $\overline{v^2} \pm 11\,\%$, $-\overline{uv} \pm 17\,\%$
Laser anemometer	U, $V \pm 0{\cdot}06$ ms; $\overline{u^2}$ and $\overline{v^2} \pm 4\,\%$ maximum profile value; $-\overline{uv} \pm 16\,\%$ maximum profile value
Thermal tuft	γ_{pu}: $\pm 0{\cdot}06$
Position from wall	$\pm 0{\cdot}05$ mm
Skin friction coefficient C_f	Ludwieg–Tillman, $\pm 6{\cdot}5\,\%$ Surface hot wire, $\pm 12\,\%$

TABLE 1. Estimated uncertainties of measured quantities

4. Experimental results

4.1. *Ensemble-averaged velocity profiles*

Ensemble-averaged velocity profiles were obtained in the unseparated upstream boundary layer and the outer part of the separated flow using single-wire and cross-wire hot-wire anemometer probes. Only the laser anemometer was used for regions where backflow occurred, $\hat{\gamma}_{pu} < 1$. In regions where both laser and hot-wire anemometers produce valid data, the results agreed within experimental uncertainties. Table 1 presents the experimental uncertainties for each measured quantity as determined by the method of Kline & McClintock (1953). While some of the profile results are shown here, Simpson *et al.* (1980*b*) present them in some detail.

Upstream of 2·7 m, the mean-velocity profiles and the mean-velocity profiles for the comparable steady free-stream flow of Simpson *et al.* (1981*a*) agree within experimental uncertainties. The ensemble-averaged velocity profiles $\hat{U}/\hat{U}_e$ *vs.* $y/\hat{\delta}_{0{\cdot}99}$ for each phase also agree with the mean profile $\overline{U}/\overline{U}_e$ *vs.* $y/\delta_{0{\cdot}99}$. Here $\delta_{0{\cdot}99}$ is the location from the test wall where $\overline{U}/\overline{U}_e = 0{\cdot}99$. The quantity $\bar{\delta}_{0{\cdot}99}$ is the cycle average of $\hat{\delta}_{0{\cdot}99}$, which is the location from the wall where $\hat{U}/\hat{U}_e$ is 0·99. In general, $\delta_{0{\cdot}99}$ is different from $\bar{\delta}_{0{\cdot}99}$ since the location on an averaged profile is not the same as the average of locations on ensemble-averaged profiles.

Figure 4 shows the first-harmonic phase angles ϕ_{1e} and $\phi_{1\log}$ for the free-stream velocity and the ensemble-averaged velocity in the semilogarithmic region respectively. Upstream of 2·7 m, $\phi_{1\log}$ is about 2°–3° lower than ϕ_{1e}. This difference is not due to experimental uncertainty. All these data show a smooth gradual increase of ϕ_1 from the semilogarithmic region to the free stream. The ratio $\tilde{U}_1/\overline{U}$ of the first harmonic to the mean velocity was closely equal to 0·3 or $\tilde{U}_{1e}/\overline{U}_e$ from the semilogarithmic region to the outer edge of the boundary layer at these upstream locations. As in the free stream, the second and third harmonics had amplitudes of about 2 % of the first harmonic.

Figure 5 shows the measured phase angle ϕ_1 for $\tilde{U}_1$ at 1·33 m. Nearer the wall than the semi logarithmic region ϕ_1 is as much as 50° lower than ϕ_1 in the semilogarithmic region. The nearest wall data indicate that ϕ_1 approaches a value near $\phi_{1\log}$ at the wall. As discussed in appendix B, this large measured phase lead of $\tilde{U}_1$ near the wall in the viscous sublayer is apparently due to very small oscillations of the hot-wire probe relative to the test wall at the flow oscillation frequency. Data at all locations upstream of 2·8 m show this effect. As pointed out in appendix B, near detachment this effect is very small. Figure 5 shows that the phase angle for $\widetilde{u_1^2}$ also varies greatly in the viscous sublayer. As discussed in §4.2, u-spectra in the viscous sublayer do not show any unusual behaviour. The wall shear-stress phase angle appears to be nearly

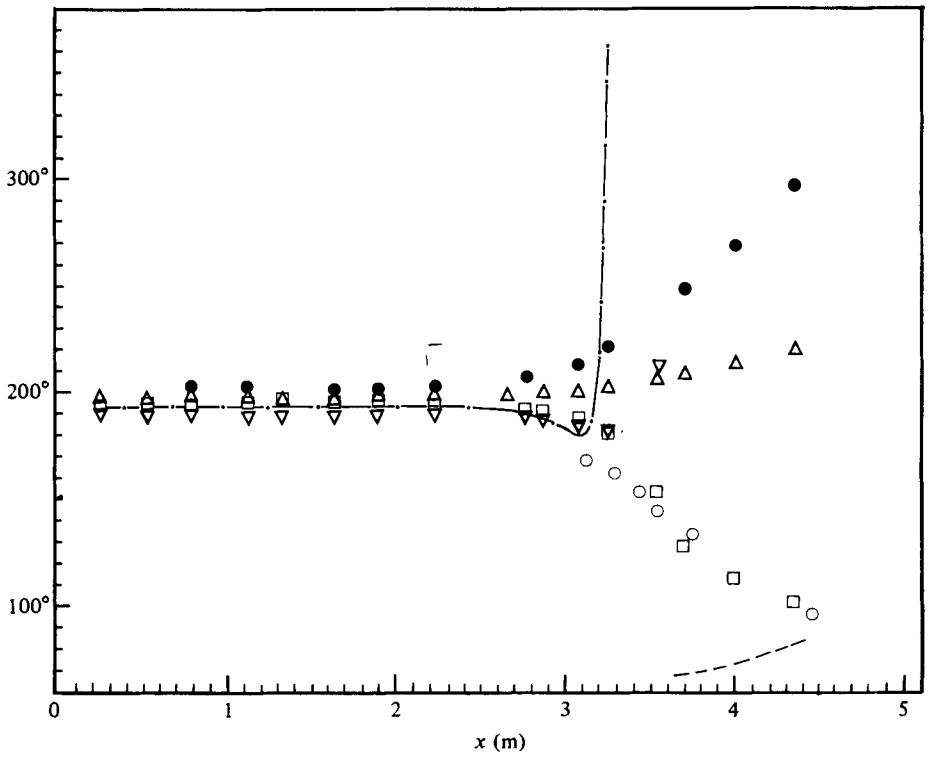

FIGURE 4. Phase angles of first harmonics: △, ϕ_{1e}, free-stream velocity; □, $\phi_{1\log}$, semilogarithmic velocity region; ▽, ϕ_{1N}, wall shearing stress; ○, λ_1, fraction of time flow moves downstream; ●, $\lambda_{1\tilde{u}^2}$, in semilog region. Line denotes phase angle of wall shear stress calculated by the quasisteady method of Cousteix *et al.*

equal to $\phi_{1\log}$, as discussed in §4.4. Thus the large phase leads measured in the near-wall region appear to be apparatus-dependent.

Downstream of 2·7 m, where the pressure-gradient relaxation begins, $\phi_{1\log}$ is progressively less than upstream values, while ϕ_{1e} increases as shown in figure 4. As shown in figure 6, the ensemble-averaged velocity profiles $\hat{U}/\hat{U}_e$ *vs.* y for each phase at 2·85 m have a slightly different shape. Figures 6(*a*) and 7 show that the ensemble-averaged velocities near the wall lead the free-stream oscillation by a few degrees. Figure 8 shows that $\tilde{U}_1/\overline{U}$ is in excess of 0·4 in the semilogarithmic velocity-profile region, while $\tilde{U}_{1e}/\overline{U}_e$ is still about 0·3.

Figure 9 shows that $\overline{U}/\overline{U}_e$ *vs.* $y/\delta_{0.99}$ profiles for the steady and unsteady flows have different shapes downstream of 2·7 m. Figures 10 and 11 show large phase-angle ϕ_1 variations through the downstream detached flow and show that $-\widetilde{uv}_1$ and $\tilde{U}_1$ are closely in phase while $\widetilde{u}_1^2$ and $\widetilde{v}_1^2$ are very much out of phase with $\tilde{U}_1$. These phase variations are not due to small oscillations of the laser-anemometer probe volume relative to the wall. The phase angles are nearly constant in the inner 0·1–0·2 of the detached shear layer where mean backflow is observed in figure 9.

As shown in figure 8, $\tilde{U}_1/|\overline{U}|$ increases to values of unity and greater in this mean backflow region. The second harmonic to mean ratio $\tilde{U}_2/|\overline{U}|$ has nearly uniform values in the inner 20 % of the shear layer downstream of the beginning of detachment, with values of about 0·03, 0·05, 0·15, 0·15 and 0·15 at 3·06 m, 3·23 m, 3·68 m, 3·97 m and 4·34 m respectively. The phase angle ϕ_2 is scattered and has values of $100° \pm 60°$,

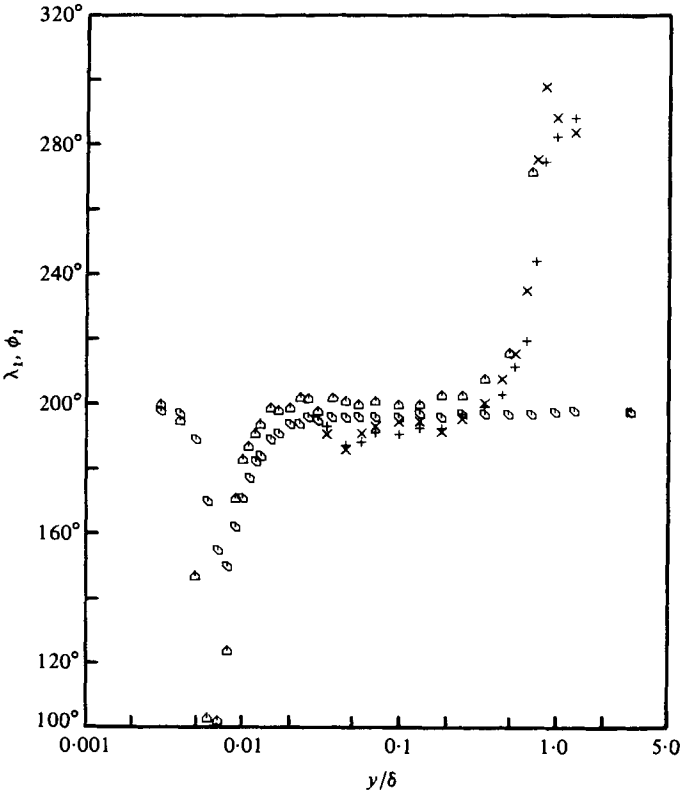

FIGURE 5. Phase angles of first harmonics at 1·34 m: ○, $\tilde{U}_1$ and △, $\widetilde{u_1^2}$ from single-wire data; +, $\widetilde{v_1^2}$ and ×, $-\widetilde{uv}_1$ from cross-wire data. Note logarithmic abscissa.

$140° \pm 40°$, $140° \pm 20°$, $160° \pm 20°$ and $180° \pm 10°$ at these locations. In the outer region $\tilde{U}_2/\bar{U}$ decreases from the near-wall value to 0·03 or less in the free stream. These data indicate that a closely quasisteady upstream flow with small phase variations develops large amplitude and phase variations during detachment.

4.2. *Turbulence quantities*

Figures 12, 14 and 16 compare the profiles of several mean turbulence quantities for the steady and unsteady flows. Upstream of 2·7 m, $(\overline{u})^{\frac{1}{2}}/\bar{U}_e$ profiles measured by the single-wire probe are in very good agreement for both flows. Differences between $(\overline{v^2})^{\frac{1}{2}}/\bar{U}_e$ profiles and between $-\overline{uv}/\bar{U}_e$ profiles obtained by the cross-wire probe for each flow are within experimental uncertainties.

Downstream of detachment $\overline{u^2}$ and $\overline{v^2}$ are higher for the unsteady flow than the steady flow, especially near the wall where mean backflow occurs. The $-\overline{uv}/\bar{U}_e^2$ profile at 3·5 m shows a large discrepancy in the outer region, which is apparently due to anomalous LDV data. At the same location there is very good agreement of steady and unsteady flow data near the wall. The seeding concentration and LDV data rate were much better near the wall than in the outer region, so these data are more reliable.

Figures 13, 15 and 17 show that $\widetilde{u_1^2}/\overline{u^2}$, $\widetilde{v_1^2}/\overline{v^2}$ and $-\widetilde{uv}_1/\overline{uv}$ are about 0·5–0·6 in the inner half of the boundary layer upstream of 2·7 m. Downstream, unsteady effects cause $-\widetilde{uv}_1/\overline{uv}$ to increase to values near 0·7 near the wall, while $\widetilde{u_1^2}/\overline{u^2}$ and $\widetilde{v_1^2}/\overline{v^2}$ remain near 0·5.

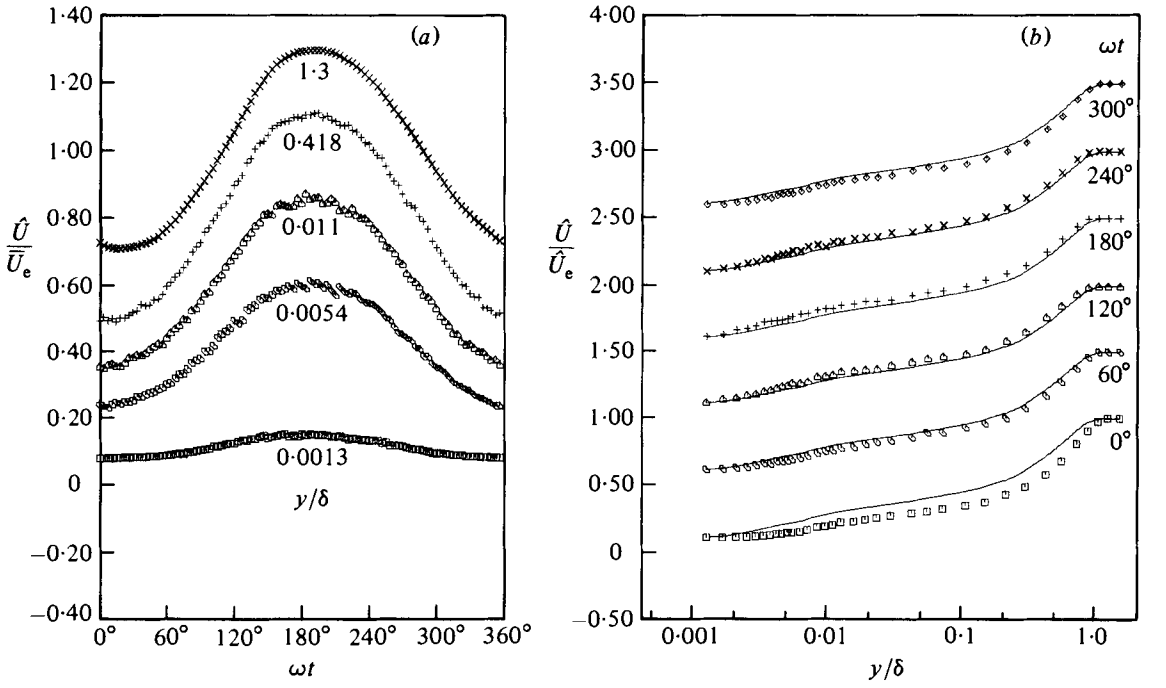

FIGURE 6. Phase-averaged data at 2·85 m: (*a*) $\hat{U}/\bar{U}_e$ *vs.* ϕ_1 at several y/δ positions; (*b*) $\hat{U}/\hat{U}_e$ *vs.* y/δ at several ϕ_1.

Figure 4 shows that the phase angle for $\widetilde{u_1^2}$ in the backflow near the wall is progressively greater than the free-stream velocity phase angle downstream of detachment. The phase angle for $\widetilde{v_1^2}$ near the wall is about 20° less than the phase angle for $\widetilde{u_1^2}$ downstream of detachment, while $-\widetilde{uv}_1$ lags $\tilde{U}_1$ by about 20°. At the location of maximum $\overline{u^2}$ across the shear layer, the phase angle for $\tilde{u}_1^2$ is progressively greater than the phase angle for $\tilde{U}_1$ downstream of detachment. This indicates that the turbulence structure progressively lags the ensemble-averaged flow oscillation downstream of the beginning of detachment.

Figures 5, 7, 10 and 11 show that the phase angles λ_1 for $\tilde{u}_1^2$, $-\widetilde{uv}_1$ and $\widetilde{v_1^2}$ increase to large values in the outer region. This is due to the intermittent turbulent–non-turbulent interface that oscillates up and down at about 180° out of phase with the free-stream velocity oscillation.

If the measured phase shifts near the wall of the first harmonic of $\tilde{U}$ and $\widetilde{u^2}$ were real fluid-dynamical effects rather than instrumentation induced upstream of separation, then the turbulence spectra may show some unusual distributions. The spectra of the u-velocity fluctuation at various phases of a cycle were examined in the near-wall region. The FFT and phase-selector circuit mentioned in §2 were used to determine ensemble-averaged spectra over each of 8 phase ranges of 45° each for a cycle.

Each ensemble-averaged spectrum $\hat{F}(n)$ that was obtained possessed a n^{-1} region in the range of $1 < \hat{U}_e/n\delta < 10$. At turbulence spectral frequencies above and below the n^{-1} range, $n\hat{F}(n)$ monotonically decreased toward zero. This spectral behaviour is typical near the wall for steady boundary layers and indicates no special effect of periodic unsteadiness.

Ensemble-averaged turbulence kinetic-energy diffusion fluxes $\frac{1}{2}\widehat{u^2v}$ and $\frac{1}{2}\widehat{v^3}$ were measured with the cross-wire anemometer and electronics mentioned in §2.3 in order

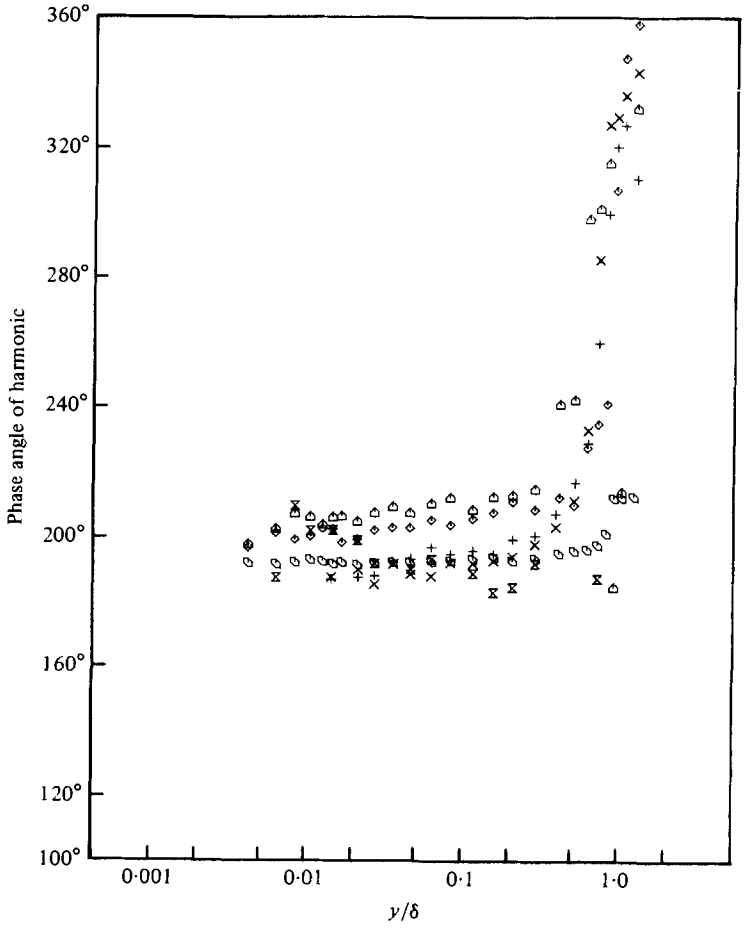

FIGURE 7. Phase angles of first harmonics. From LDV data at 2·85 m: ○, $\tilde{U}_1$; △, $\widetilde{u_1^2}$; ◆, $\widetilde{v_1^2}$; ⧗, $-\widetilde{uv}_1$. From cross-wire data at 2·83 m: +, $\widetilde{v_1^2}$; ×, $-\widetilde{uv}_1$.

to determine how periodic unsteadiness affects turbulence diffusion. Experimental uncertainties for these fluxes were less than $\pm 25\,\%$, as was the case for the measurements of Simpson *et al.* (1981*a*) for the comparable steady free-stream separating flow.

Upstream of detachment, the same type of mean profiles occur for both the steady and unsteady cases. For regions farther from the wall than the maximum shearing stress, these fluxes are positive, indicating that the turbulence-diffusion flux is away from the wall. The mean results for the steady and unsteady flows agree within experimental uncertainties, so no effect of periodic unsteadiness was detected upstream of detachment.

Downstream of detachment, measurements were made only in the outer region. The mean fluxes indicated agreement with the steady-flow results. The streamwise distributions of $\overline{U_e(\delta_{0\cdot995}-\delta^*)}$ were the same for the steady and unsteady flows within experimental uncertainties, which indicates that the unsteadiness has no large effect on the mean entrainment velocity $\overline{V}_p$:

$$\overline{V}_p = \frac{d}{dx}(\overline{U_\infty(\delta_{0\cdot995}-\delta^*)}) \approx 2\left(\frac{\overline{pv}}{\rho}+\tfrac{1}{2}\overline{q^2V}\right)/\overline{q^2}. \tag{4.1}$$

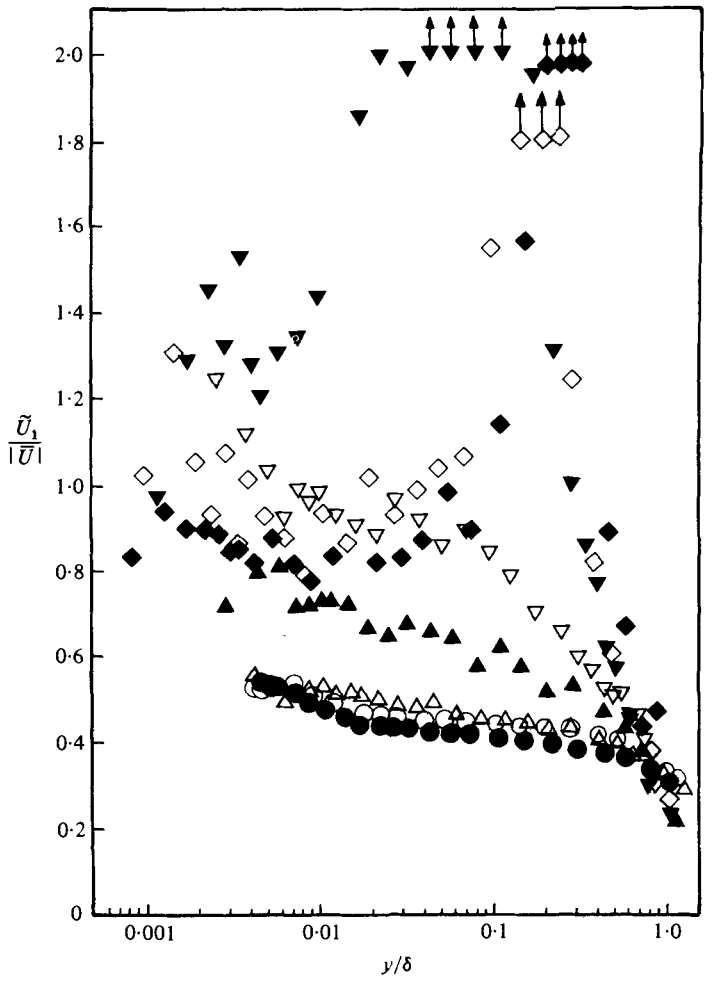

FIGURE 8. $\tilde{U}_1/|\overline{U}|$ *vs.* y/δ near detachment and downstream. Hot-wire: ●, 2·74 m; ○, 2·85 m. LDV: △, 2·85 m; ▲, 3·06 m; ▽, 3·23 m; ▼, 3·66 m; ◇, 3·97 m; ◆, 4·32 m.

Since the mean entrainment velocity $\overline{V}_p$ is proportional to the turbulence kinetic-energy flux, as shown in this equation, this supports the conclusion that periodic unsteadiness has little effect on the mean turbulence-diffusion processes in the outer region. In both the steady and unsteady flows, turbulence diffusion became an increasingly important transport mechanism during detachment and downstream.

The first harmonic of each diffusion flux was approximately in phase with the first harmonics of $\tilde{U}$, $\widetilde{u^2}$, $\widetilde{v^2}$ and $-\widetilde{uv}$ upstream of detachment. Of course, no diffusion-flux data were obtained with the cross-wire downstream of detachment near the wall, where the first harmonics of these quantities are not in phase. The ratio $(\widetilde{u^2v}_1+\widetilde{v_1^3})/(\overline{u^2v}+\overline{v^3})$ of the amplitude of the first harmonic to the mean increases as detachment is approached and downstream, as in the case of these other measured quantities.

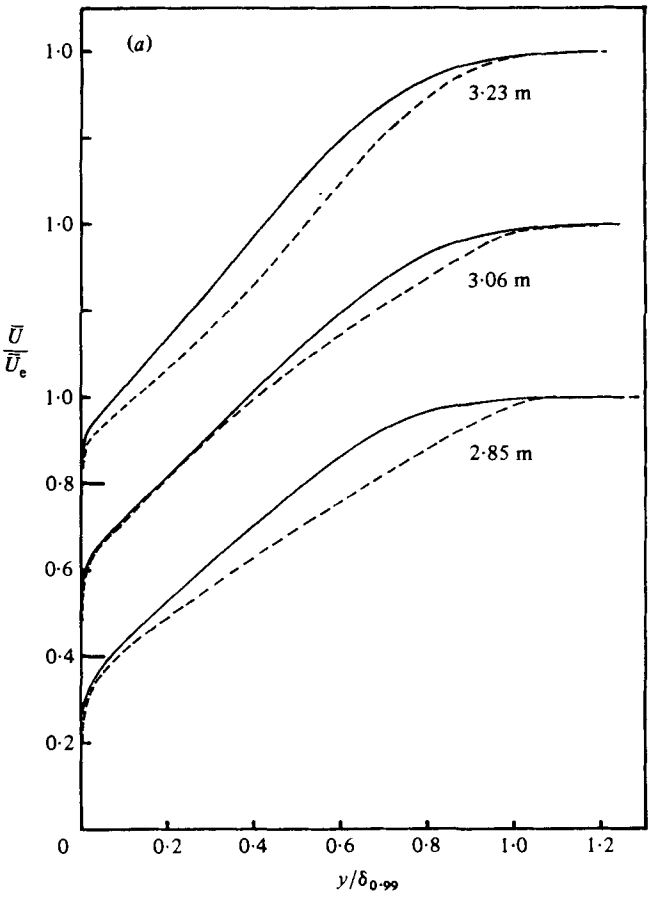

FIGURE 9(*a*). For caption see p. 238.

4.3. *Upstream–downstream intermittency*

Figure 18 and figures 5, 6 and 7 of Shivaprasad & Simpson (1982) show the ensemble-averaged values of the fraction of time that the flow moves downstream γ_{pu} at 1·22 mm from the wall for a cycle at several streamwise locations. These values were obtained using the thermal-tuft and LDV measurements. The LDV results were obtained from the relation

$$\hat{\gamma}_{pu} = \frac{1}{2}\left[1 + \mathrm{erf}\left(\frac{\hat{U}}{(2\hat{u^2})^{\frac{1}{2}}}\right)\right] \tag{4.2}$$

and values of $\hat{U}$ and $\hat{u^2}$ measured with the LDV. Simpson (1976) showed that this relation, which is derived from Gaussian velocity-probability distribution, closely correlated directly measured values of γ_{pu}.

Figure 19 shows the cycle-averaged values $\bar{\gamma}_{pu}$ near the wall for the unsteady and steady flows. The steady-flow thermal-tuft results are between 0·05 and 0·1 higher than the LDV results, as noted in §2.5. For the unsteady flow the average of the results from both thermal-tuft orientations closely agrees with the LDV results. $\bar{\gamma}_{pu}$ near the wall for the unsteady flow is higher than for the steady flow downstream of 3·4 m, indicating that the mean-flow behaviour for the steady and unsteady detached flows is distinctly different. The unsteady-flow detachment process begins

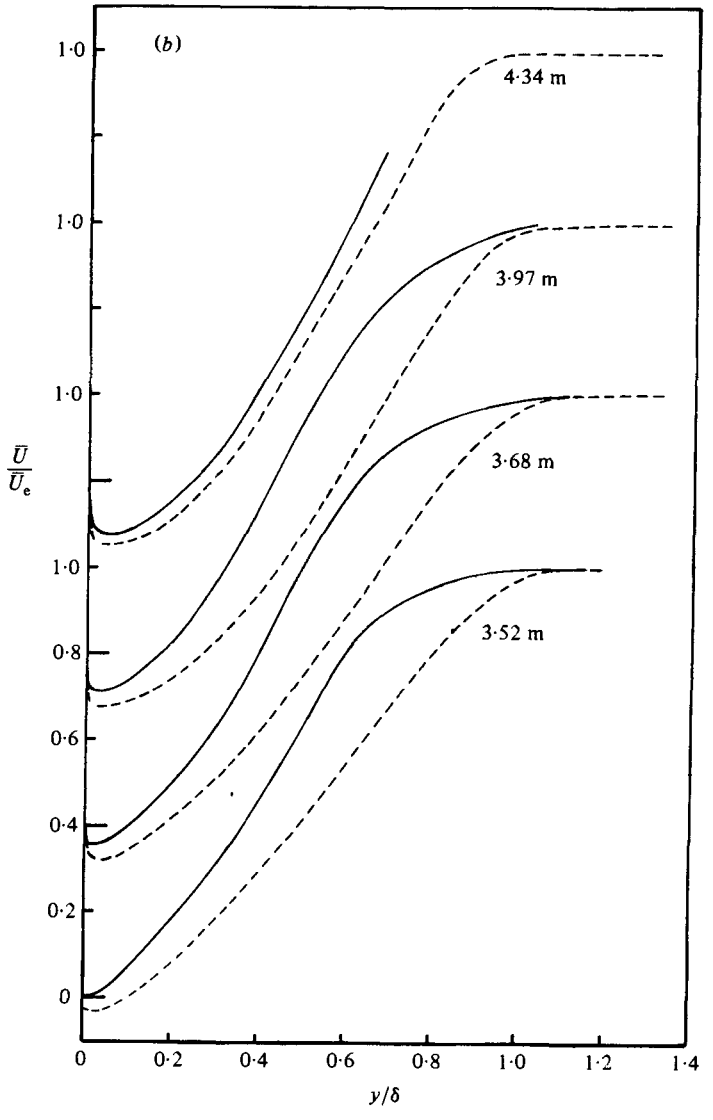

FIGURE 9. $\bar{U}/\bar{U}_e$ *vs.* y/δ. ——, mean unsteady velocity profile; – – –, steady-flow mean velocity profiles of Simpson *et al.* (1981*a*). Note displaced ordinates.

upstream of where it began for the steady free-stream flow. Downstream, significant pressure gradient relaxation continues until near 3·5 m, where $\bar{\gamma}_{pu\,\min} \approx 0{\cdot}5$ and the free-stream pressure gradient and velocity are in phase (figure 2).

Although $\hat{U}$ and $\widehat{u^2}$ have nearly a sinusoidal variation near the wall, figure 18 and (4.2) show that $\hat{\gamma}_{pu}$ is not described by a single harmonic variation. Nevertheless, the phase angle λ_1 for the first harmonic $\tilde{\gamma}_{pu1}$ is nearly in phase with $\tilde{U}_1$ downstream of 3·1 m, as shown in figure 4. This phase angle λ_1 nearly coincides with the phase at which $\hat{\gamma}_{pu}$ is a maximum at locations downstream of 3·4 m.

4.4. *Skin-friction results*

Figure 20 shows mean flow skin-friction coefficients $\frac{1}{2}\overline{C_f} = \bar{\tau}_w/\rho\bar{U}_e^2$ for the unsteady flow and the comparable steady flow of Simpson *et al.* (1981*a*). The Ludwieg–Tillman

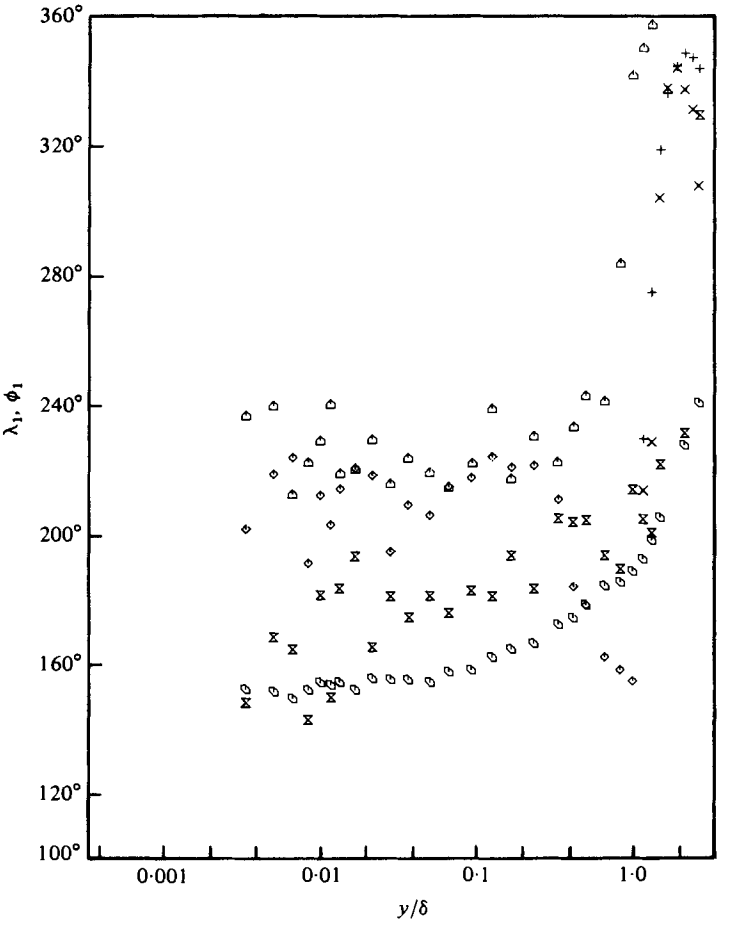

FIGURE 10. Phase angles of first harmonics at 3·52 m. From LDV data: ⬡, $\tilde{U}_1$; ⌂, $\widetilde{u_1^2}$; ◇, $\widetilde{v_1^2}$; ⧗, $-\widetilde{uv}_1$. From cross-wire data: +, $\widetilde{v_1^2}$; ×, $-\widetilde{uv}_1$.

and Preston-tube results are for the steady flow, while the surface hot-wire results are for the unsteady flow. The surface hot-wire results for the steady flow agreed with the Ludwieg–Tillman results except very close to detachment (Simpson *et al.* 1981*a*). Figure 21 shows the ratio $\tilde{\tau}_{w1}/\bar{\tau}_w$ amplitude to mean surface skin friction measured from the surface hot wire.

Upstream of 2·7 m, $\tilde{\tau}_{w1}/\bar{\tau}_w$ is nearly constant at about $\frac{2}{3}$ within $\pm 12\,\%$ uncertainty. $\bar{\tau}_w$ agrees with the steady-flow results upstream of about 2 m. Nearer detachment, $\bar{\tau}_w$ from the surface hot wire is higher than the Ludwieg–Tillman and Preston-tube results, as was the case for the steady flow. Figure 4 shows that the phase angle ϕ_{1w} for the first harmonic is nearly constant at 190° upstream of 2·7 m, and is only about 5° lower than the phase angle in the semilogarithmic region. Nearer detachment, ϕ_{1w} decreases, as does $\phi_{1\log}$.

Downstream of 2·7 m, $\tilde{\tau}_{w1}/\bar{\tau}_w$ decreases. If the Ludwieg–Tillman results are used for $\bar{\tau}_w$, $\tilde{\tau}_{w1}/\bar{\tau}_w$ is about $\frac{2}{3}$ near detachment. Downstream of 3 m, $\hat{\gamma}_{pu}$ is less than unity during part of a cycle, indicating intermittent backflow. Thus the surface hot-wire results are suspect downstream of this location because of signal-rectification effects due to flow-direction reversal.

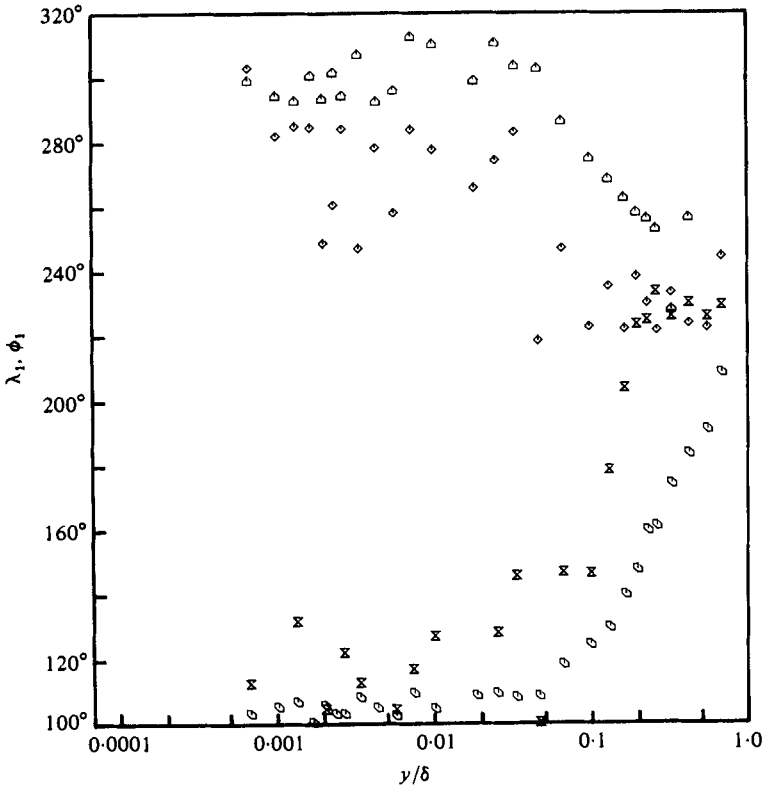

FIGURE 11. Phase angles of first harmonics at 4·34 m from LDV data: ○, $\hat{U}_1$; △, $\widetilde{u_1^2}$; ◇, $\widetilde{v_1^2}$; ⧗, $-\widetilde{uv}_1$.

5. Discussion

5.1. *Ensemble-averaged and mean velocities*

Figure 22 shows the mean-velocity profiles in $\overline{U}^+$ *vs.* $\log_{10}|\overline{y}^+|$ coordinates upstream of detachment when surface hot-wire mean-skin-friction values are used. Upstream of 2·7 m these results agree with the steady-flow equation

$$\overline{U}^+ = \frac{1}{K}\ln|\overline{y}^+| + C \tag{5.1}$$

with $K = 0{\cdot}41$ and $C = 5{\cdot}0$, which Simpson *et al.* (1981*a*) found to hold upstream of any flow reversal. Farther downstream, the results fall below this relationship. If the Ludwieg–Tillman skin-friction values shown in figure 20 are used at these latter locations, better agreement results.

Based upon dimensional grounds, Simpson (1977) proved that the phase-angle variation of the ensemble-averaged oscillation velocity is zero within a semilogarithmic region. If, as in the steady free-stream case, one set of velocity scales and lengthscales exists for the velocity profile near the wall ($\hat{U}_\tau$ and $\nu/\hat{U}_\tau$) and another set exists near the free stream ($\hat{U}_e$ and $\hat{\delta}$), then the velocity profile in a common overlap region is given by

$$\hat{U} = \hat{U}_\tau b\left(\frac{y\hat{U}_\tau}{\nu}, \omega t - \phi_{\text{inner}}\right) \tag{5.2}$$

or

$$\hat{U} = \hat{U}_\infty g\left(\frac{y}{\hat{\delta}}, \omega t - \phi_{\text{outer}}\right). \tag{5.3}$$

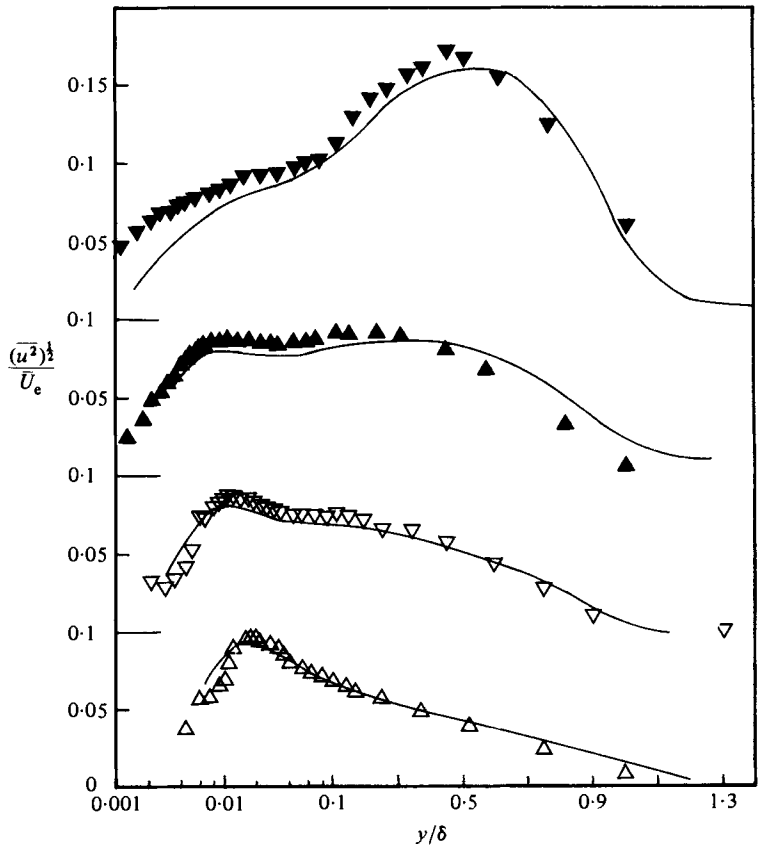

FIGURE 12. Streamwise mean turbulence-intensity profiles for the unsteady flow, $(\overline{u^2})^{\frac{1}{2}}/\bar{U}_e$ *vs.* y/δ: △, 0·79 m; ▽, 2·2 m; ▲, 2·74 m; ▼, 3·66 m. Profiles for the steady flow are given by the solid lines. Note the log-linear abscissa and displaced ordinates.

In this overlap region both relations should produce the same result:

$$\frac{\hat{U}_\tau^2}{\nu}\frac{\partial b}{\partial \hat{y}^+} = \frac{\partial \hat{U}}{\partial y} = \frac{\hat{U}_\infty}{\delta}\frac{\partial g}{\partial (y/\delta)}. \tag{5.4}$$

Since this overlap region is formally independent of viscosity, $\partial b/\partial \hat{y}^+$ must vary as $1/\hat{y}^+$. Thus b, g and $\hat{U}$ vary with $\ln|y|$. Only if ϕ is independent of y can this be satisfied. Figures 5 and 7 and the many phase-angle plots presented by Simpson *et al.* (1980*b*) verify this result.

If the semilogarithmic equation (5.1) is valid for the ensemble-averaged velocity at each phase of a cycle, the velocity phase angle must be the same as that for the wall shear stress. For this low-frequency moderate-amplitude oscillation experiment this is approximately the case, as shown in figure 4. Using (5.1) and a single oscillation harmonic

$$\hat{U}_\tau = \bar{U}_\tau(1 + A_{\tau w1}\cos(\omega t - \phi_{w1}))^{\frac{1}{2}} \tag{5.5}$$

($A_{\tau w1} = \tilde{\tau}_{w1}/\bar{\tau}_w$) one can obtain the ensemble-averaged velocity

$$\frac{\hat{U}}{\bar{U}_\tau} = (1 - \tfrac{1}{16}A_{\tau w1}^2)\left\{\frac{1}{K}\ln|\bar{y}^+| + C\right\} + \tfrac{3}{256}A_{\tau w1}^4 + \tfrac{1}{2}A_{\tau w1}\left(\frac{1}{K}\ln|\bar{y}^+| + C + 1 + \frac{1}{K} - \frac{3}{16}\frac{A_{\tau w1}^2}{K}\right)\cos(\omega t - \phi_{w1}). \tag{5.6}$$

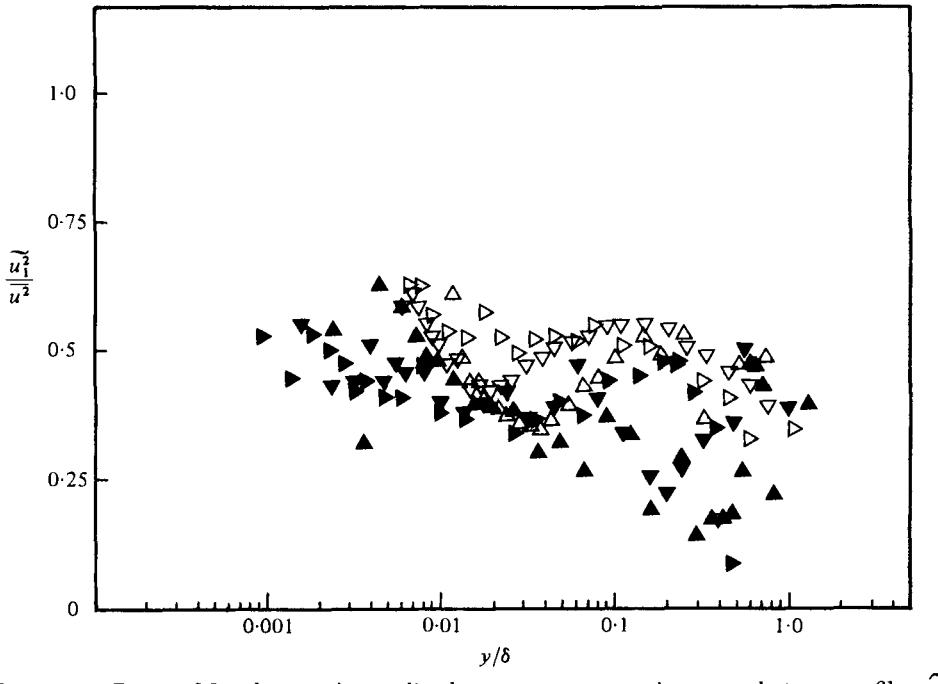

FIGURE 13. Ratio of first harmonic amplitude to mean streamwise normal-stress profiles, $\widetilde{u_1^2}/\overline{u^2}$ *vs.* y/δ; △, 0·79 m; ▽, 2·2 m; ▷, 2·74 m; ▲, 3·23 m; ▼, 3·52 m; ▶, 3·97 m. Note logarithmic abscissa.

Using an experimental value for $A_{\tau w1}$ of about $\frac{2}{3}$ from figure 21, the mean part of (5.6) is

$$\overline{U}^+ = \frac{35}{36K}\ln|y^+| + \frac{35C}{36} + \frac{1}{432K}. \tag{5.7}$$

This indicates only a 3% change in the slope and intercept of the mean-flow semilogarithmic equation as compared with the steady-flow equation (5.1). This small difference is well within the uncertainty of the results shown in figure 22.

The ratio of the amplitude of the first harmonic to mean velocity $\tilde{U}_1/\overline{U}$ from (5.6) is in good agreement with data in the semilogarithmic region upstream of 2·74 m. This is consistent with the fact that upstream of 2·74 m the ensemble-averaged velocity profile $\hat{U}/\hat{U}_e$ for each phase is closely the same as the time-mean profile. Nearer detachment, the measured $A_{\tau w1}$ decreases so that values of $\tilde{U}_1/\overline{U}$ calculated from (5.6) are less than those upstream, while measured values are greater. If values of $A_{\tau w1}$ of $\frac{2}{3}$ are used near detachment, as discussed in §4.4, then (5.6) produces $\tilde{U}_1/\overline{U}$ values nearer measured values.

Upstream of detachment where the flow behaves in a quasi-steady manner for each phase of the cycle, the analysis of Houdeville & Cousteix (1979, 1981) can be used to calculate ϕ_{1w} and $A_{\tau w1}$ from the mean flow and $\tilde{\delta}^*/\bar{\delta}^*$, ϕ_{δ^*1}, $\tilde{\theta}_1/\bar{\theta}$, $\phi_{\theta 1}$, $\tilde{U}_{e1}/\overline{U}_e$ and ϕ_{1e}. Houdeville & Cousteix began with the steady-flow result that is derived from the velocity-defect relation:

$$\left(\frac{1}{\frac{1}{2}\overline{C}_f}\right)^{\frac{1}{2}} = \frac{1}{K}\ln\left|\frac{\overline{U}_e\bar{\delta}^*}{\nu}\right| + \overline{D}^*, \tag{5.8}$$

$$\overline{D} = 2\overline{G} - 4{\cdot}25\overline{G}^{\frac{1}{2}} + 2{\cdot}12, \quad \overline{G} = \frac{(\overline{H}-1)}{\overline{H}(\frac{1}{2}\overline{C}_f)^{\frac{1}{2}}}.$$

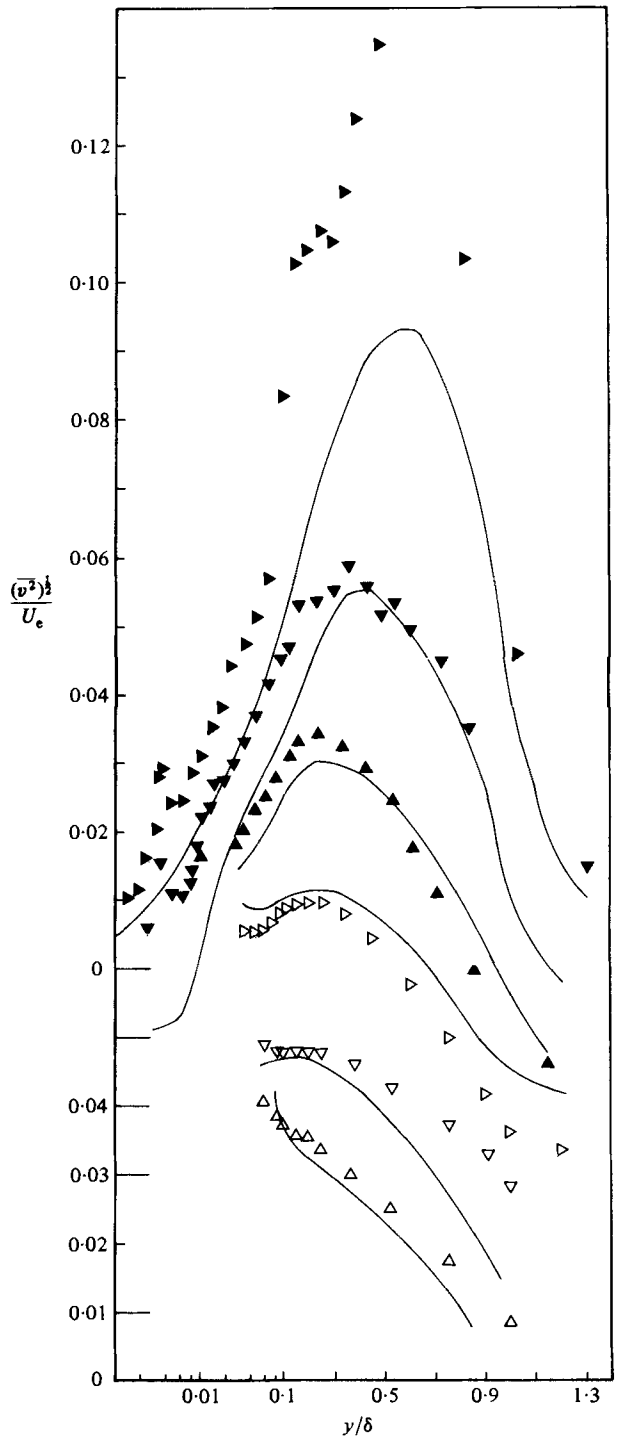

FIGURE 14. Normal-to-wall mean turbulence intensity profiles for the unsteady flow, $(\overline{v^2})^{\frac{1}{2}}/\overline{U}_e$ *vs.* y/δ: △, 0·79 m; ▽, 1·63 m; ▷, 2·19 m; ▲, 2·67 m; ▼, 3·23 m; ▶, 3·97 m. Profiles for the steady flow are given by the solid lines. Note the log-linear abscissa and displaced ordinates.

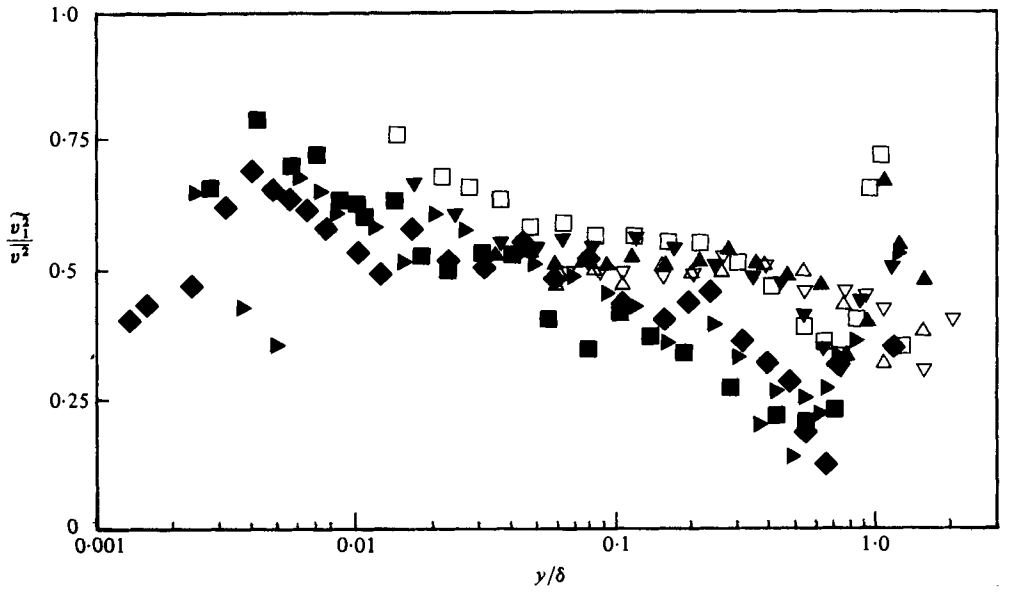

FIGURE 15. Ratio of first-harmonic amplitude to mean normal-to-wall normal stress profiles, $\tilde{v}_1^2/\overline{v^2}$ *vs.* y/δ; △, 0·79 m; ▽, 1·63 m; ▲, 2·19 m; ▼, 2·67 m; □, 2·82 m; ■, 3·05 m; ▶, 3·23 m; ◆, 3·51 m.

Substituting phase-averaged quantities into these equations and expanding the result produces terms for the oscillatory flow in addition to (5.8). Houdeville & Cousteix showed that calculated ϕ_{1w} values were in very good agreement with the data of Patel (1977), Cousteix *et al.* (1977), and Houdeville & Cousteix (1979) for ϕ_{1u} in the semilogarithmic velocity-profile region, except in the presence of flow reversal.

Figures 4 and 21 show that ϕ_{1w} and $A_{\tau w1}$ are well predicted by these equations upstream of 2·2 m. Nearer detachment, ϕ_{1w} is well predicted as long as there is no flow reversal. Calculated $A_{\tau w1}$ values near detachment are higher than the experimental values shown in figure 21. However, as noted in §4.4 and in the discussion above, $A_{\tau w1}$ values near detachment without flow reversal should be about $\frac{2}{3}$ in order to be consistent with (5.1) and (5.6). Considering the uncertainty of measured $A_{\tau w1}$ values near detachment, the quasisteady method of Houdeville & Cousteix produces good results as long as there is no flow reversal.

Perry & Schofield (1973) proposed universal empirical mean-velocity-profile correlations for the inner and outer regions of adverse-pressure-gradient boundary layers near separation. Their correlations apply to all types of adverse pressure gradient boundary layers irrespective of whether they are in equilibrium or not, but with the restriction that the ratio $(-\overline{uv})_{max}/U_\tau^2$ must exceed 1·5. Simpson *et al.* (1981*a*) found that their steady free-stream data agreed with these correlations. Here these correlations are compared with the present unsteady-flow data to determine their validity.

The Perry & Schofield defect law for the outer flow is

$$\frac{U_e - U}{U_s} = f_2(\eta_2), \quad \text{where} \quad \eta_2 = \frac{y}{\Delta}, \tag{5.9}$$

$$\Delta = \frac{U_e}{U_s}\frac{\delta^*}{C}. \tag{5.10}$$

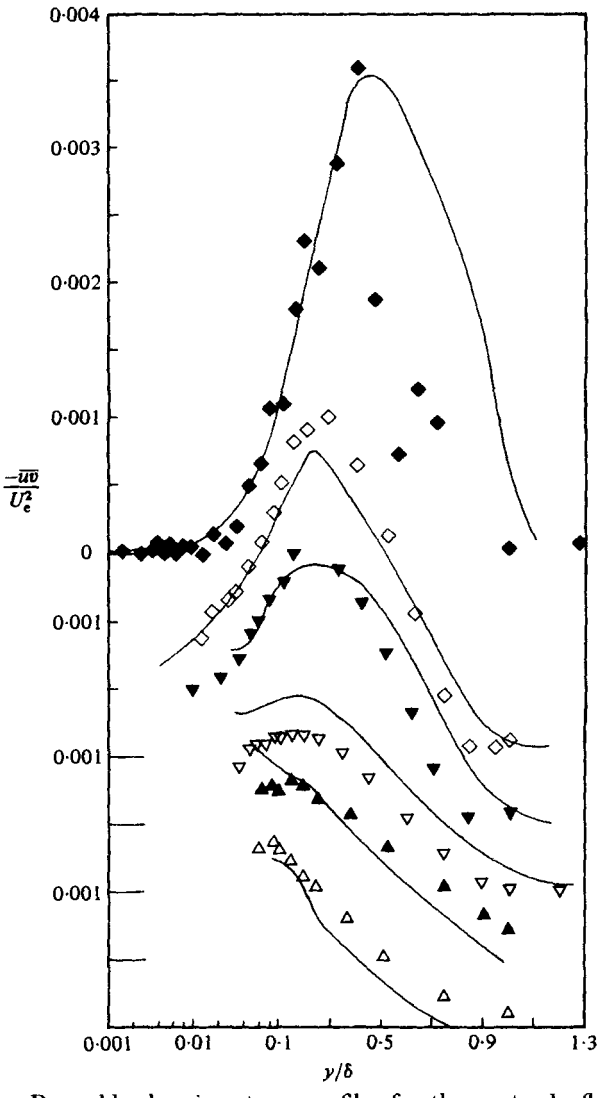

FIGURE 16. Mean Reynolds shearing-stress profiles for the unsteady flow, $-\overline{uv}/\overline{U}_e^2$ *vs.* y/δ: △, 0·79 m; ▲, 1·63 m; ▽, 2·20 m; ▼, 2·67 m; ◇, 2·82 m; ◆, 3·51 m. Profiles for the steady flow are given by the solid lines. Note the log-linear abscissa and displaced ordinates.

C is a constant given by $C = \int_0^\infty f_2(\eta_2)\, d\eta_2$ and found empirically to be equal to 0·35. The inner law was defined as

$$\frac{U}{U_\tau} - h = f_1(\eta_1), \quad \eta_1 = \frac{y}{e}, \quad e = \frac{Lu_\tau^2}{U_M^2}, \tag{5.11}$$

where h is a constant, U_M^2 is the maximum shear stress and L is the distance from the wall to the maximum shear stress. Near the wall, (5.11) takes the form of (5.1).

The condition for the overlap between the inner and the outer regions leads to the following relations:

$$\frac{U}{U_e} = 0{\cdot}47\left(\frac{U_s}{U_e}\right)^{\frac{3}{2}}\left(\frac{y}{\delta^*}\right)^{\frac{1}{2}} - \frac{U_s}{U_e} + 1, \tag{5.12}$$

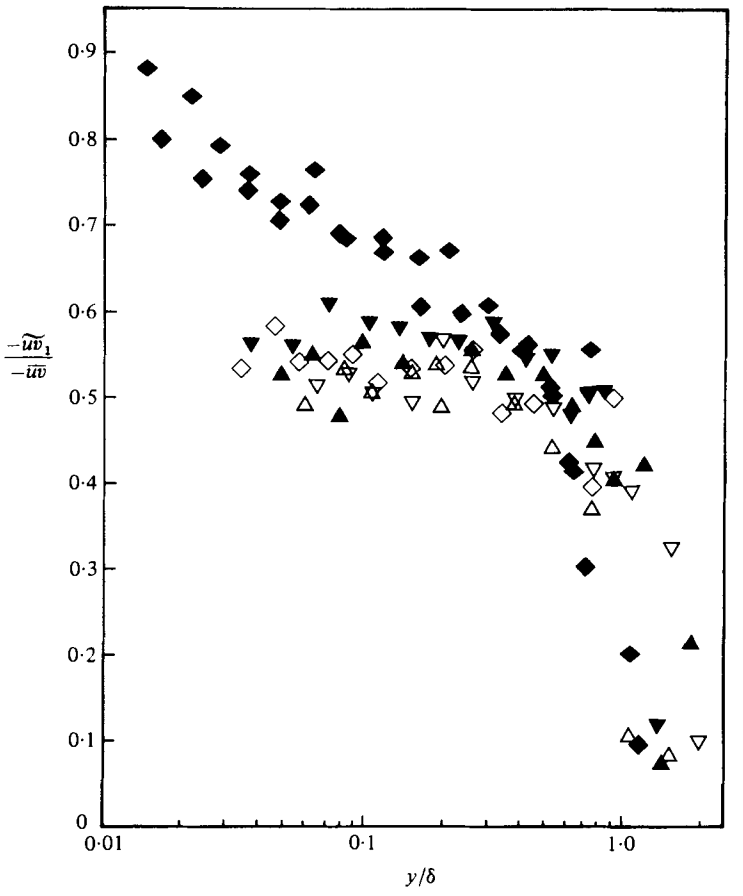

FIGURE 17. Ratio of first-harmonic amplitude to mean Reynolds shearing-stress profiles, $-\widetilde{uv}_1/-\overline{uv}$ *vs.* y/δ: △, 0·79 m; ▲, 1·234 m; ▽, 1·63 m; ▼, 1·90 m; ◇, 2·20 m; ◆, 2·67 m; ◆, 2·82 m.

$$f_1(\eta_1) = 6{\cdot}4\eta_1^{\frac{1}{2}}, \tag{5.13}$$

$$\frac{U_S}{U_M} = 8\left(\frac{\Delta}{L}\right)^{\frac{1}{2}}. \tag{5.14}$$

Equation (5.12) is used to obtain the experimental values of the velocity scale U_s from a plot of U/U_e *vs.* $(y/\delta^*)^{\frac{1}{2}}$ with U_s/U_e as a parameter.

Downstream of 2·67 m, $(-\widehat{uv})_{max}/\hat{U}_\tau > 1{\cdot}5$ was satisfied by the present unsteady-flow data. Figure 23 shows outer-region results for the steady free-stream flow of Simpson *et al.* (1981*a*), mean and ensemble-averaged velocity profiles for the present flow, and the tabulated correlation of $f_2(\eta_2)$ presented by Schofield (1980). Steady-flow and mean unsteady-flow profiles are almost coincident upstream of 3 m and differ from the tabulated correlation within the scatter of data used to obtain the correlation. Ensemble-averaged profiles at 2·72 m are about 0·05 lower than the correlation near $y/\hat{\Delta} = 0{\cdot}4$ at large phase angles, while at 2·85 m they are about 0·05 lower near $y/\hat{\Delta} = 0{\cdot}7$ at small phase angles.

In the lower part of figure 23, the shaded region denotes the steady, mean unsteady, and ensemble-averaged profiles downstream of 3 m when no flow reversal is present, i.e. $\hat{\gamma}_{pu} = 1$. While these profiles agree with the tabulated correlation within experimental uncertainties, they have a more concave shape in the middle region than

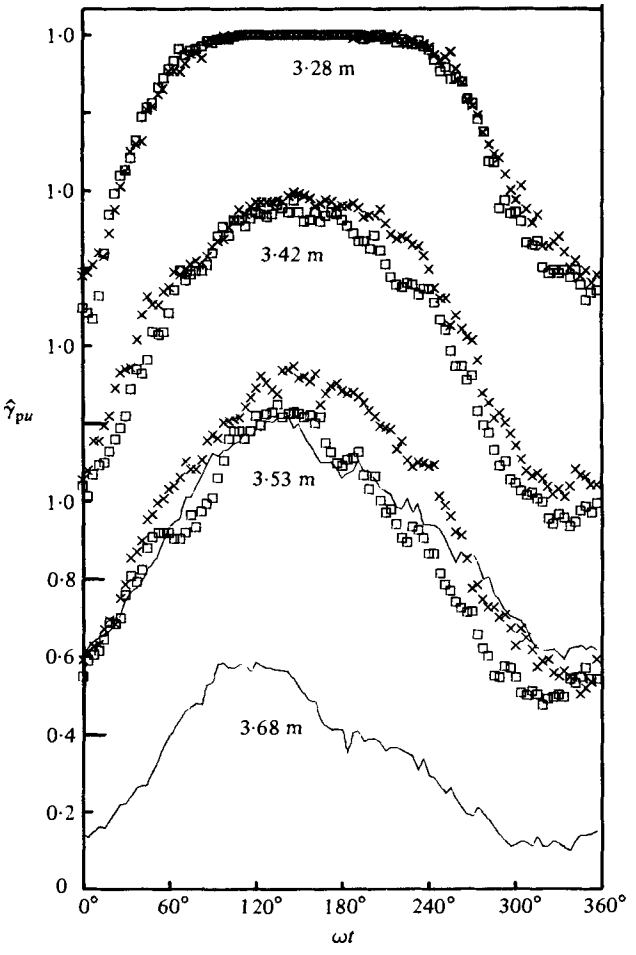

FIGURE 18. Phase-averaged $\hat{\gamma}_{pu}$ measured 1·22 mm from the wall *vs.* ωt. Thermal tuft: □, one orientation; ×. orientation reversed. ——, from $\hat{U}$ and $\hat{u}^2$ LDV measurements and (4.2). Note displaced ordinates.

the profiles upstream of 3 m. When $\hat{\gamma} < 1$, the ensemble-averaged profiles differ appreciably from the tabulated correlation, as demonstrated by the data in figure 23 for 0° at 3·06 m.

Figure 24 shows that the results from the mean and ensemble-averaged unsteady-flow profiles agree with (5.14) within the scatter of the data used by Perry & Schofield when $\hat{\gamma}_{pu} \approx 1$. When $\hat{\gamma}_{pu} < 1$, the results do not agree with this correlation, such as is shown by the data for 3·06 m at the right. Counterclockwise hysteresis loops for phase-averaged profiles for each location near detachment indicate that the data do show some non-quasisteady behaviour. Ensemble-averaged velocity profiles which agree best with the tabulated correlation in figure 23 produce results in figure 24 that fall just to the left of the line representing equation (5.14). This is consistent with the fact that most of the steady-flow data examined by Perry & Schofield also produce results in the same region of figure 24. Equations (5.11) and (5.13) are satisfied by the mean unsteady flow upstream of where $\bar{\gamma}_{pu} < 1$.

Since the Perry & Schofield correlations satisfy the ensemble-averaged profiles approximately when $\hat{\gamma}_{pu} = 1$, then the difference in steady and mean unsteady

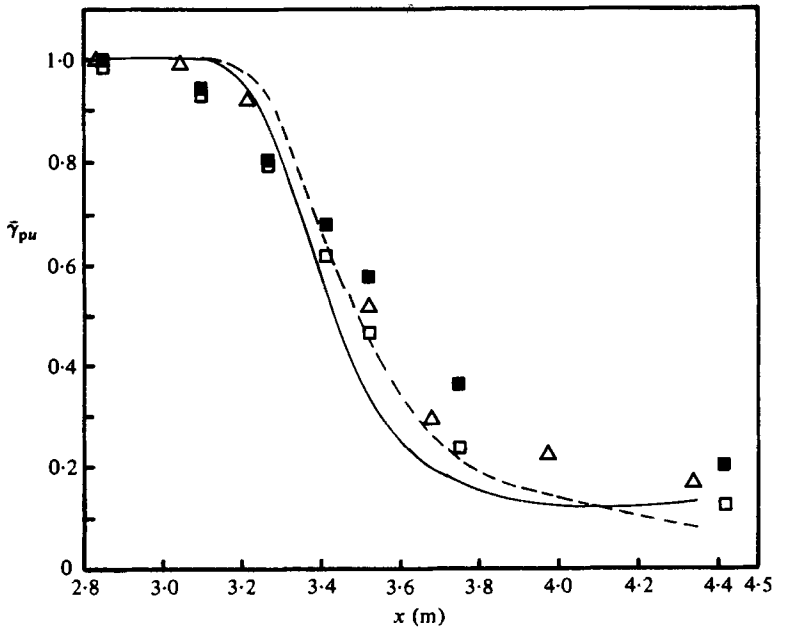

FIGURE 19. Cycle-averaged $\bar{\gamma}_{pu}$ measured 1·22 mm from the wall along the centreline of the test wall. Thermal tuft: □, one orientation; ■, orientation reversed. △, $\overline{U}$ and $\overline{u^2}$ LDV measurements and (4.2). ——, – – –, direct LDV and thermal tuft measurements for the Simpson *et al.* (1981*a*) steady free-stream flow.

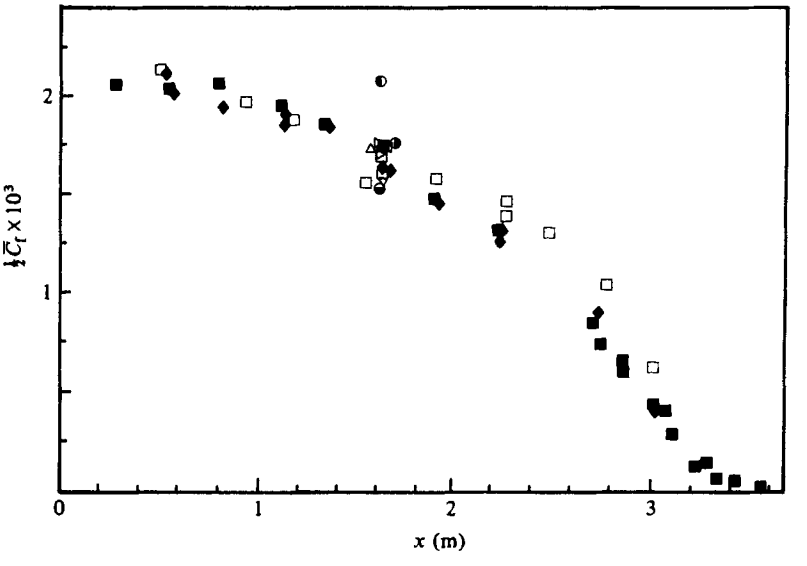

FIGURE 20. Mean-flow friction factor $\frac{1}{2}\overline{C}_f$ versus x: □, surface hot-wire gauge. Steady free-stream case: ■, Ludwieg–Tillman; ◆, Preston tube.

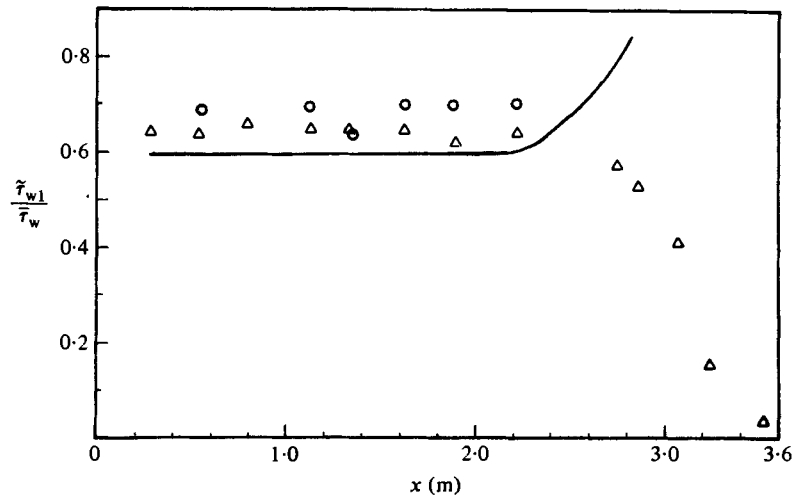

FIGURE 21. Ratio of first-harmonic amplitude to mean surface shearing stresses, $\tilde{\tau}_{w1}/\bar{\tau}_w$ *vs.* x: symbols for experiments on two different days; solid line calculated by quasi-steady model of Cousteix *et al.*

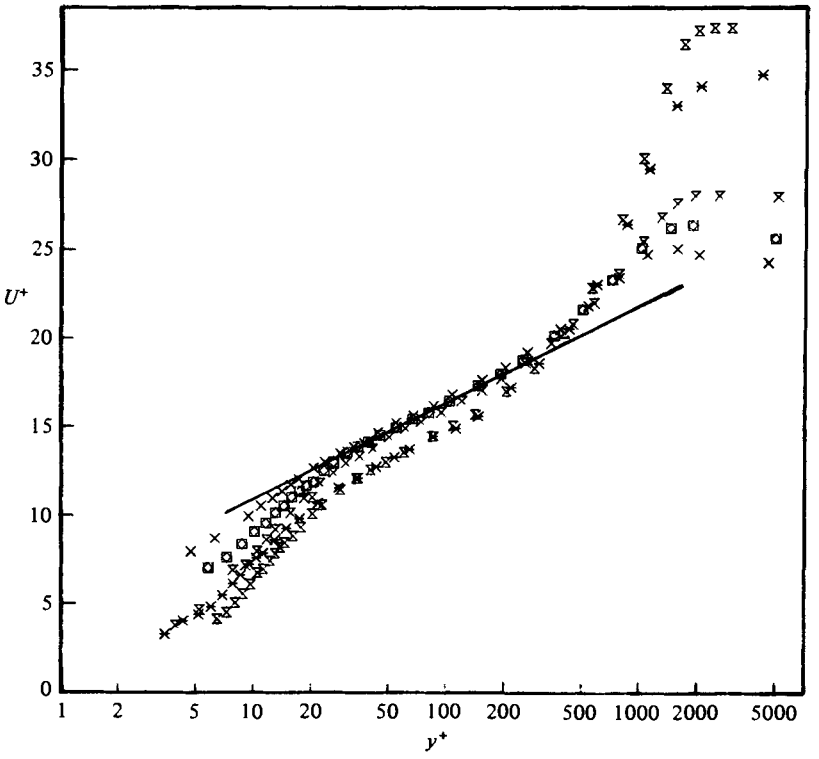

FIGURE 22. Mean flow law-of-the-wall velocity profiles, $\bar{U}^+$ *vs.* $\log_{10} y^+$: ×, 1·63 m; ⊠, 1·89 m; ⧖, 2·22 m; ⋇, 2·74 m; ⧗, 2·85 m. ——, (5.1).

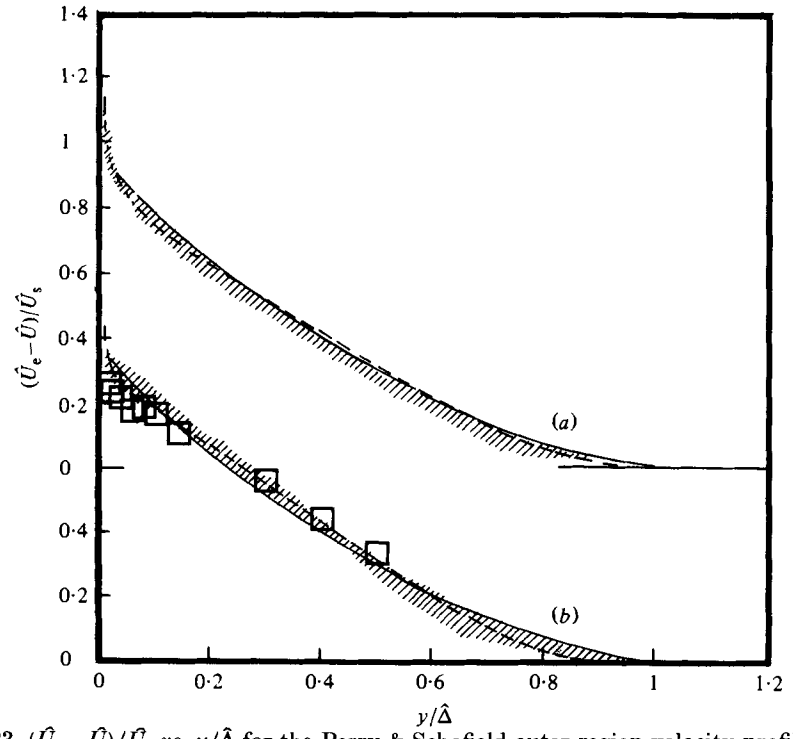

FIGURE 23. $(\hat{U}_e-\hat{U})/\hat{U}_s$ *vs.* $y/\hat{\Delta}$ for the Perry & Schofield outer-region velocity-profile correlation upstream of detachment. ——, tabulated values from Schofield (1980). – – – –, steady flow (Simpson *et al.* 1981*a*) data in (*a*) at 2·70 m and 2·85 m and in (*b*) at 3·01 m. Shaded area in (*a*) from phase-averaged unsteady-flow profiles at 2·74 m and 2·85 m and in (*b*) from phase-averaged unsteady- and steady-flow profiles at 3·06 m and 3·23 m when $\hat{\gamma}_{pu\,min} > 0{\cdot}8$. In (*b*), □ show results at 3·06 m, $\omega t = 0°$, $\hat{\gamma}_{pu\,min} = 0{\cdot}8$.

profiles shown in figure 9 is due to averaging quasisteady profiles of varying-thickness boundary layers over a cycle. This averaging produces a slightly different outer-region profile shape and higher δ/δ^* values for the mean unsteady flow. To some extent the difference between steady and mean unsteady profiles downstream of detachment is also due to averaging phase-averaged profiles with varying-thickness shear layers over a cycle.

Even though large phase variations exist through the downstream detached shear flow and the flow at all phases is not quasisteady, phase-averaged profiles for a given value of $\hat{\gamma}_{pu\,min}$ are compared in figure 25 with the steady detaching flow profiles of Simpson *et al.* (1981*a*) at the same $\gamma_{pu\,min}$ value. The basis for this comparison is the steady-flow result that the velocity-profile shape factor H is closely related to $\gamma_{pu\,min}$, as discussed in §5.2. For each $\hat{\gamma}_{pu\,min}$ value shown, there is good agreement of $\hat{U}/\hat{U}_e$ *vs.* y/δ^* phase-averaged profiles with steady-flow profiles when $\partial\hat{U}_e/\partial t < 0$ and $\partial\hat{\gamma}_{pu\,min}/\partial t \leqslant 0$. Since the pressure gradient is almost in phase with $\hat{U}_e$ in the detached-flow zone, $\partial(d\hat{P}/dx)/\partial t < 0$ during these phases.

When $\partial\hat{U}_e/\partial t$ and $\partial\hat{\gamma}_{pu\,min}/\partial t$ are of opposite sign, phase-averaged profiles do not agree with the steady profile for the same $\gamma_{pu\,min}$ value. For phases when agreement is not good, the velocity profiles are higher than the steady-flow profile in the outer and middle regions and sometimes lower near the wall. For the case with $\hat{\gamma}_{pu\,min} = 0{\cdot}12$, $\partial\hat{U}_e/\partial t < 0$ whenever such a low value of $\gamma_{pu\,min}$ occurs, so no data are available for other $\partial U_e/\partial t$ conditions. These results indicate that, when the free stream is

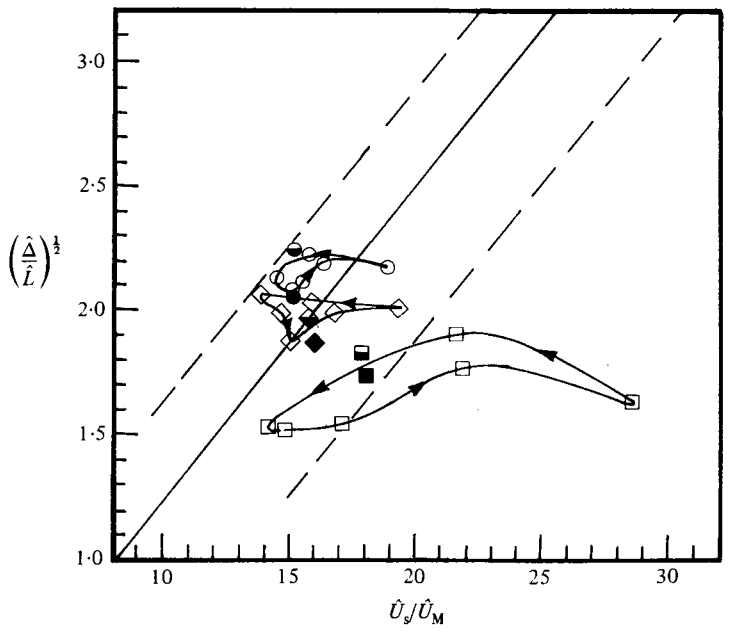

FIGURE 24. Perry & Schofield relation between velocity and shear-stress profile parameters, $\hat{U}_s/\hat{U}_m$ *vs.* $(\hat{\Delta}/\hat{L})^{\frac{1}{2}}$. Values for phase-averaged profiles at 0°, 60°, 120°, 180°, 240° and 300° of the cycle: ○, 2·74 m; ◇, 2·85 m; □, 3·06 m. Counterclockwise solid-line loops connect phase-averaged values; 0° at right-hand side of each loop. Solid symbols denote values obtained for the mean profile values. The steady-flow data used by Perry & Schofield are in the region between the dashed lines.

decelerating and flow reversal near the wall is occurring at an increasing fraction of time, the ensemble-averaged flow behaves in a quasisteady manner.

As noted in §1.2, the mean backflow in the steady free-stream case scales on the maximum negative mean velocity U_N and its distance N from the wall, as shown in figure 26. The mean backflow appears to be divided into three layers: a viscous layer nearest the wall that is dominated by the turbulent flow unsteadiness, but with little Reynolds shearing-stress effect; an intermediate layer that seems to act as an overlap region between the viscous wall and outer regions; and the outer backflow region that is really part of the large-scaled outer-region flow. For locations downstream of detachment, a semilogarithmic region described by

$$\frac{U}{|U_N|} = -0{\cdot}3 \ln \left|\frac{y}{N}\right| + B \tag{5.15}$$

seems to exist for $0{\cdot}02 < y/N < 0{\cdot}15$, where B is a constant.

This backflow does not come from far downstream but appears to be supplied intermittently by large-scale structures as they pass the separated flow, as suggested by Simpson *et al.* (1981*b*). The Reynolds shearing stresses in this region must be modelled by relating them to the turbulence structure and not to local mean-velocity gradients. The mean-velocity profiles in the backflow are a result of time-averaging the large turbulent fluctuations.

Figure 4 shows that the ensemble-averaged velocity in the backflow of the unsteady flow leads the free-stream velocity by a large amount. Even so, the backflow mean-velocity profile shapes for the unsteady flow are approximately the same as for the comparable steady free-stream case. Figures 10 and 11 show that the phase angle ϕ_{u1} does not vary appreciably with y in the nearest wall region. Far downstream

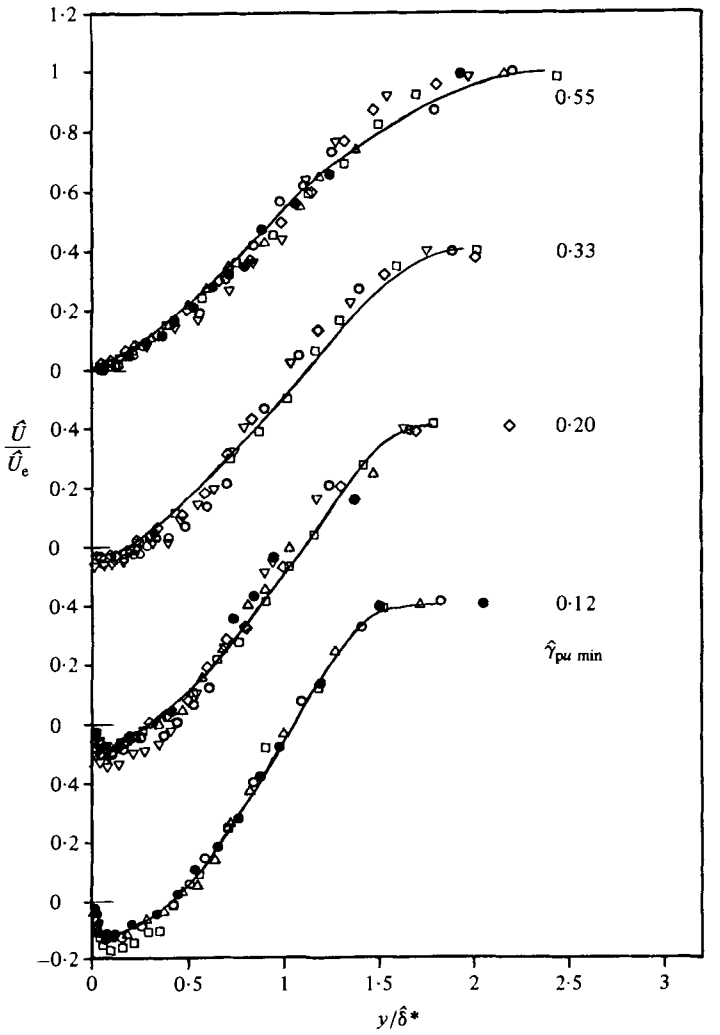

FIGURE 25. Phase-averaged velocity profiles $\hat{U}/\hat{U}_e$ *vs.* $y/\hat{\delta}^*$ *for several values of* $\hat{\gamma}_{pu\,min}$. ——, profiles from the steady flow of Simpson *et al.* (1981 *a*) at the same $\gamma_{pu\,min}$ value. Streamwise position and phase of cycle ωt given for each profile; asterisk denotes good agreement with steady-flow results. Data for $\hat{\gamma}_{pu\,min} = 0{\cdot}55$: ●, 3·23 m, *11·25°; △, 3·23 m, *326°; ○, 3·52 m, 64°; □, 3·52 m, *233°; ▽, 3·68 m, 90°; ◇, 3·68 m, 142°. Data for $\hat{\gamma}_{pu\,min} = 0{\cdot}33$: ○, 3·68 m, 49°; □, 3·68 m, *229°; ▽, 3·97 m, 56°; ◇, 3·97 m, 161°. Data for $\hat{\gamma}_{pu\,min} = 0{\cdot}20$: ●, 3·52 m, 0°; △, 3·52 m, *334°; ○, 3·68 m, 19°; □, 3·68 m, *270°; ▽, 3·97 m, 19°; ◇, 3·97 m, *221°. Data for $\hat{\gamma}_{pu\,min} = 0{\cdot}12$: ●, 3·68 m, *300°; △, 3·68 m, *338°; ○, 3·97 m, *285°; □, 3·97 m, 345°

where the ensemble-averaged velocity is always negative, ϕ_{u1} and $\tilde{U}_1/\overline{U}$ are nearly independent of y for $y < N$. Note that $\tilde{U}_1/\overline{U}$ is near unity. Thus it appears that the ensemble-averaged flow near the wall behaves like a quasisteady flow when normalized on $\hat{U}_N$ and $\hat{N}$.

Figure 4 shows that the ensemble-averaged velocity in the backflow has a progressively greater phase lead as one proceeds downstream. If the flow nearest the wall is governed by viscosity and the oscillating and mean pressure gradients, then the solution to the unsteady vorticity equation

$$\frac{\partial \omega_z}{\partial t} = \nu \frac{\partial^2 \omega_z}{\partial y^2} \tag{5.16}$$

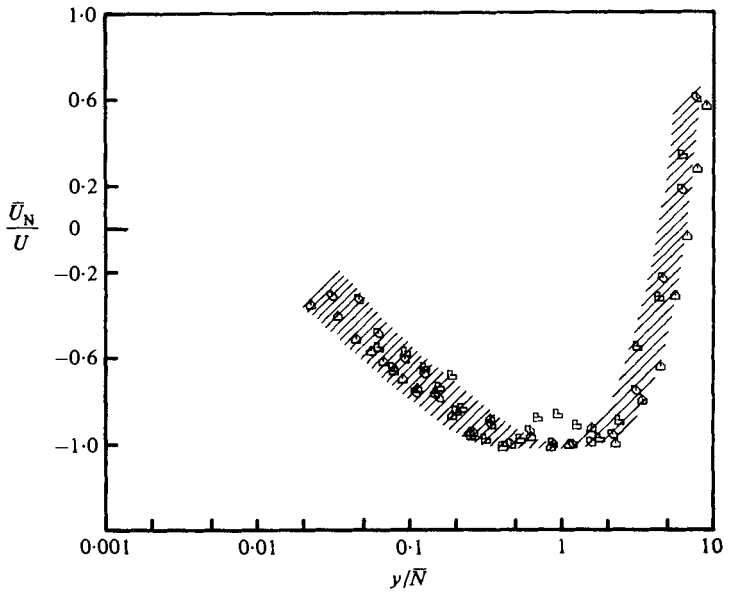

FIGURE 26. Normalized backflow mean-velocity profiles for the unsteady flow: ⊔, 3·68 m; ⊃, 3·97 m; ⌂, 4·34 m. Shaded region denotes data from the steady flow of Simpson *et al.* (1981*a*).

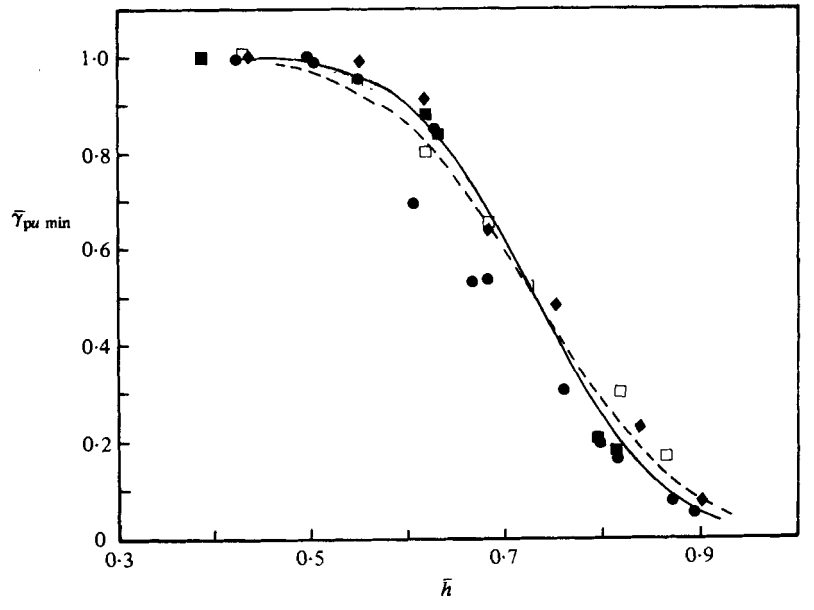

FIGURE 27. $\bar{\gamma}_{pu\,min}$ *vs.* $\bar{h}$ results. Steady flow: ■, LDV data (Simpson *et al.* 1977); ●, LDV data; ◆, $\bar{\gamma}_{pu}$ from thermal tuft (Simpson *et al.* 1981*a*). Mean unsteady flow, $\bar{\gamma}_{pu}$ from thermal tuft: ■. Equation (5.17) with $\bar{h} = 0{\cdot}73$: ——, $\sigma = 0{\cdot}10$; – – –, $\sigma = 0{\cdot}12$.

indicates that the near-wall velocity oscillation leads the pressure gradient oscillation by 135°. Figure 4 shows that ϕ_{u1} near the wall approaches this 135° lead near the downstream location where measurements ceased.

5.2. *Flow detachment and upstream–downstream intermittency* γ_{pu}

Kline, Bardina & Strawn (1981) presented a proposed correlation for steady flow that relates the near-wall minimum fraction of time that there is forward flow, $\gamma_{pu\,\min}$, to the shape factor $H = \delta^*/\theta$ in the vicinity of detachment. Figure 27 presents the correlation in a normalized form using $(H-1)/H = h$. The steady free-stream data of Simpson *et al.* (1977, 1981*a*) and values from the mean unsteady flow fall along a single region, with the exception of 3 low LDV data points from Simpson *et al.* (1981*a*). Kline *et al.* (1981) showed that the data of Ashjaee & Johnston (1980) for a diffuser and Eaton & Johnston (1980) for a reattaching flow also fall in this region.

The apparent reason that this correlation is fairly good for flows with some backflow is that the shape of the mean velocity profiles is related to the turbulence structure of the entire shear layer. In other words, similar $\overline{u^2}$, $\overline{v^2}$ and $-\overline{uv}$ structures which produce $\overline{u^2}$ near the wall also determine similar U profiles. Thus $\overline{u^2}$ and U near the wall strongly determine γ_{pu} (Simpson 1976), while the mean-velocity profile determines θ, δ^* and H.

Most of the LDV data on figure 27 are closely fitted by

$$\gamma_{pu} = \tfrac{1}{2}\operatorname{erfc}\left(\frac{h-\bar{h}}{\sqrt{2}\,\sigma}\right), \tag{5.17}$$

with $\bar{h} = 0{\cdot}73$ and $\sigma = 0{\cdot}1$. As shown in figure 27, $\sigma = 0{\cdot}12$ is a poorer fit, especially for γ_{pu} near unity and near zero. With $\sigma = 0{\cdot}1$, $h = 0{\cdot}63$ is one standard deviation away from $\gamma_{pu} = 0{\cdot}5$, which is where intermittent transitory detachment for the steady free-stream flow occurs according to the Sandborn & Kline (1961) correlation for flat and low-curvature surfaces ($H = 2{\cdot}70$). When $h = 0{\cdot}63$, γ_{pu} is 0·84, which is close to the value of 0·80 that Simpson *et al.* (1981*a*) use as a definition of intermittent transitory detachment.

Simpson *et al.* (1977, 1981*a*) point out that the attached boundary-layer structure for steady free-stream flows, as described by Perry & Schofield (1973), ceases at intermittent transitory detachment. Collins & Simpson (1978) and Kline *et al.* (1981) note that boundary-layer calculation methods fail in the vicinity of intermittent transitory detachment. As noted by Collins & Simpson such upstream calculation methods should be terminated at this location and downstream detached flow methods begun there.

Figure 28 shows the results for the unsteady flow at several streamwise locations and various phases of the oscillation cycle. Values for various phases at a given streamwise location are connected by lines with arrows to show the direction of movement during a cycle. At 3·23 m there are some phases of the cycle with very little reversed flow and others with the ensemble-averaged $\hat{\gamma}_{pu\,\min}$ as low as 0·53. A hysteresis loop occurs, but lies within the shaded region showing the steady free-stream results of figure 27. At 3·52 m and downstream there are other hysteresis loops in the $\hat{\gamma}_{pu}$ *vs.* $\hat{h}$ plane at each location. The loops become broader in the downstream direction, which reflects the fact that there is progressively more phase variation in the phase-averaged velocity and turbulence distributions. At 3·23 m there is much less breadth to the hysteresis loop because of much less phase variation within ensemble-averaged velocity and turbulence distributions.

Figure 29 presents $\hat{\gamma}_{pu}$ *vs.* x for various phases of the oscillation cycle, which clearly

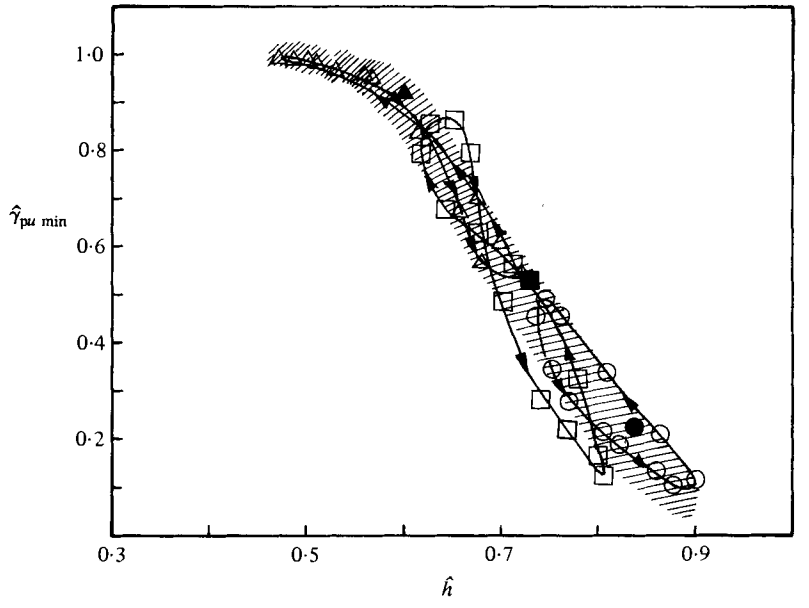

FIGURE 28. $\hat{\gamma}_{pu\,min}$ *vs.* $\hat{h}$ for the unsteady flow using the thermal tuft: △, 3·23 m; □, 3·52 m; ○, 3·97 m. Solid lines form hysteresis loops for data at given streamwise position. Shaded region denotes steady-flow results from figure 27. Solid symbols denote mean unsteady-flow results.

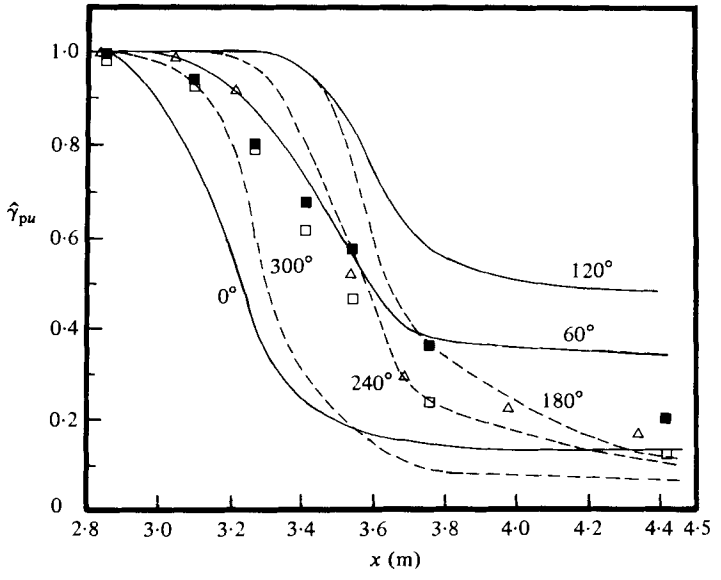

FIGURE 29. Phase-averaged $\hat{\gamma}_{pu\,min}$ *vs.* x for different phases of a cycle shown by lines. Cycle-averaged $\bar{\gamma}_{pu\,min}$ values shown by symbols and legend from figure 19.

illustrates the hysteresis of the unsteady separated flow. As the flow accelerates between 20°–120° of a cycle, the location where $\hat{\gamma}_{pu}$ is less than unity moves downstream and $\hat{\gamma}_{pu}$ increases at all downstream locations as backflow fluid is washed downstream and the shear-layer thickness decreases significantly. Since the adverse pressure gradient is also increasing, it causes progressively greater backflow at downstream locations as the free-stream flow accelerates between 120° and 180°, while $\hat{\gamma}_{pu}$ remains high upstream. After backflow occurs a large fraction of time at downstream locations, the location where $\hat{\gamma}_{pu}$ is less than unity moves upstream as the free-stream flow decelerates from the 200° value back to the minimum at 20°.

5.3. *Reynolds shearing stresses*

Upstream of detachment the Reynolds shearing stresses behave in a quasisteady manner, being in phase with the ensemble-averaged velocity and the normal stresses $\hat{u}^2$ and $\hat{v}^2$. The correlation coefficient $-\hat{uv}/\sqrt{(\hat{u}^2\hat{v}^2)}$ is also quasisteady. Equation (1.10) describes the unsteady Reynolds shearing stress in the semilogarithmic velocity-profile region within experimental uncertainties.

Downstream of detachment near the wall, $-\widetilde{uv}_1$ lags $\tilde{U}_1$ only about 20°, while $\widetilde{u}_1^2$ and $\widetilde{v}_1^2$ are substantially out of phase with $-\widetilde{uv}_1$, as shown in figures 10 and 11. Although there is some hysteresis and phase lag for the near-wall turbulence structure as noted in §4.2, the observed behaviour can be explained qualitatively by the steady-flow results of Simpson *et al.* (1981*a*).

Near the wall $\hat{\gamma}_{pu}$ is nearly in phase with $\tilde{U}_1$, as shown in figure 4, but since $\overline{U}$ is *negative* the ensemble-averaged backflow is greatest when $\hat{\gamma}_{pu}$ is low and when $\hat{u}^2$ and $\hat{v}^2$ are near maximum values. In other words, $|\hat{U}|$ in the backflow is nearly in phase with $\hat{u}^2$ and $\hat{v}^2$. This is consistent with the general observation from the steady flow that $\overline{u^2}$ and $\overline{v^2}$ are greater when there is more mean backflow.

The steady-flow results (Simpson *et al.* 1981*a*, figure 13*c*) show that $-\overline{uv}/\sqrt{(\overline{u^2}\overline{v^2})}$ decreases with decreasing $\bar{\gamma}_{pu}$. In the unsteady flow $-\hat{uv}$ is greater with less ensemble-averaged backflow or greater $\hat{\gamma}_{pu}$. In other words, $|\hat{U}|$ is lower and $\tilde{U}_1$ is nearly in phase with $-\widetilde{uv}_1$, which is consistent with the steady-flow result.

6. Conclusions – the nature of an unsteady separating turbulent boundary layer

These experiments show that a periodic unsteady separating turbulent boundary layer at a Reynolds number of $4{\cdot}7 \times 10^6$, a practical reduced frequency of 0·61, and $\tilde{U}_{1e}/\overline{U}_3 = 0{\cdot}3$ has both similarities and differences with a steady free-stream separating turbulent boundary at the same Reynolds number. Upstream of where intermittent backflow begins ($\hat{\gamma}_{pu} < 1$), the flow behaves in a quasisteady manner. Downstream there are non-quasisteady effects on the ensemble-averaged flow structure.

When $\hat{\gamma}_{pu} = 1$, the steady flow semilogarithmic law-of-the-wall velocity profile applies at each phase of the periodic flow cycle. The phase angle in the semilogarithmic region is constant since it forms an overlap region for the wall and outer-region flows. Well upstream of the detachment zone the quasisteady analysis of Houdeville & Cousteix (1979) predicts ϕ_{1w} and $\tilde{\tau}_{w1}/\bar{\tau}_w$. Nearer detachment, but with $\hat{\gamma}_{pu} = 1$, the Perry & Schofield velocity-profile correlations for the outer region fit the mean and ensemble-averaged velocity profiles. The turbulence structure upstream of where $\hat{\gamma}_{pu} < 1$ behaves in a quasisteady manner, with $\hat{u}^2$, $\hat{v}^2$ and $-\hat{uv}$ being in phase with $\hat{U}$.

These results indicate that after the beginning of detachment, large amplitude and phase variations develop. Even though $\hat{\gamma}_{pu\,\min}$ is related to the velocity profile shape factor $\hat{H}$ in approximately the same relationship as for the steady flow, unsteadiness effects produce hysteresis in this relationship. Ensemble-averaged velocity profiles agree with the steady-flow velocity profiles at the same value of $\hat{\gamma}_{pu\,\min}$ when $\partial \hat{U}_e/\partial t < 0$ and $\partial \hat{\gamma}_{pu\,\min}/\partial t \leqslant 0$. Thus, when the freestream is decelerating and flow reversal near the wall is occurring at an increasing fraction of time, the ensemble-averaged flow behaves in a quasisteady manner.

Near the wall in the backflow region, the ensemble-averaged velocity leads the free-stream velocity by a large amount. The phase angle of the periodic backflow velocity and $\tilde{U}_1/\overline{U}$ are nearly independent of y near the wall. The mean backflow profile in terms of $\overline{U}/\overline{U}_N$ and $y/\overline{N}$ is approximately the same as for the comparable steady free-stream case. Thus it appears that the ensemble-averaged backflow near the wall behaves like a quasisteady flow when normalized on $\hat{U}_N$ and $\hat{N}$.

Downstream of detachment $\overline{u^2}$ and $\overline{v^2}$ are slightly higher for the unsteady flow than the steady flow, especially near the wall where mean backflow occurs. The phase angle for $\widetilde{u_1^2}$ in the backflow is progressively greater than the free-stream velocity phase angle as the flow moves downstream. The turbulence structure progressively lags the ensemble-averaged flow oscillation with $-\widetilde{uv}_1$ lagging $\tilde{U}_1$ in the backflow by about 20°. The ratio $-uv_1/-\overline{uv}$ increases from about 0·5 upstream of detachment to about 0·7 downstream. As in the steady free-stream flow, $-\widehat{uv}/(\widehat{u^2}\widehat{v^2})^{\frac{1}{2}}$ decreases with decreasing $\hat{\gamma}_{pu}$, although there is some hysteresis and phase lag for the unsteady flow.

The detailed flow can be described by the following cycle of events. As the free-stream velocity begins to increase, the Reynolds shearing stresses increase, the detached shear layer decreases in thickness, and the fraction of time $\hat{\gamma}_{pu}$ that the flow moves downstream increases at all downstream locations as backflow fluid is washed downstream. As the free-stream velocity nears the maximum value, the increasingly adverse pressure gradient causes progressively greater near-wall backflow at downstream locations, while $\hat{\gamma}_{pu}$ remains high at the upstream part of the detached flow. After the free-stream velocity begins to decelerate, the detached shear layer grows in thickness, and the location where $\hat{\gamma}_{pu}$ is less than unity moves upstream. This cycle is repeated as the free-stream velocity again increases.

As a separate result from this work, it appears that measured phase shifts in the viscous sublayer can be due to small probe and test-wall oscillations at the periodic frequency.

This work was supported by the U.S. Army Research Office under Grant DAAG29-76-G-0187 and the National Aeronautics and Space Administration, Ames Research Center, under Grant NSG-2354. The authors would like to thank Messrs E. Bowles, G. Kokolis, J. Sallas, J. Yen, and Dr R. E. Nasburg for their aid in this research.

Appendix A. The effect of flow-oscillation frequency variation or 'jitter' on measurements

When the frequency of flow oscillation is not constant, but has 'jitter' as pointed out in §2.2 above, an error will be introduced in turbulent-fluctuation measurements. In the acquisition of data mentioned above, there is no jitter in the reference or clock square waves used to trigger data acquisition. Here an approximate analysis is given to show that the effect of flow jitter is negligible for the experiments and ensemble-averaged data reported here.

Consider the ideal instantaneous signal

$$\mathscr{F} = \bar{F} + \tilde{F} + f, \tag{1.2}$$

where there is no jitter. When jitter is present

$$\mathscr{F}_j = \bar{F} + \left(\tilde{F} + \frac{\partial \tilde{F}}{\partial \omega}(\delta\omega)\right) + \left(f + \frac{\partial f}{\partial \omega}(\delta\omega)\right), \tag{A 1}$$

where first-order Taylor series expansions denote the effects of frequency variation $\delta\omega$ on the periodic and turbulent oscillations. It is assumed that the jitter does not produce strong nonlinear effects in the flow.

For a given phase of the cycle the ensemble-average (1.1) of this signal is

$$\hat{F}_j = \bar{F} + \tilde{F} + \frac{1}{N}\sum_{n=1}^{N}\left[\left(\frac{\partial \tilde{F}}{\partial \omega}\right)\delta\omega + f + \left(\frac{\partial f}{\partial \omega}\right)\delta\omega\right]. \tag{A 2}$$

The summation of each term in the square brackets is zero because of: the average frequency variation $\delta\omega$ is zero, the ensemble-averaged turbulent fluctuation $\tilde{f}$ is zero by definition, and there is no correlation between the turbulent fluctuation and the jitter, respectively. Thus, the jitter has no effect on ensemble-averaged values:

$$\hat{F} = \hat{F}_j = \bar{F} + \tilde{F}. \tag{A 3}$$

The ensemble-averaged variance of $\mathscr{F}_j$ from $\hat{F}_j$ is obtained in the data-acquisition procedure and is the apparent mean-squared turbulent fluctuation that includes the effect of jitter

$$\widehat{(\mathscr{F}_j - \hat{F}_j)^2} = \frac{1}{N}\sum_{n=1}^{N}\left[\left(\frac{\partial \tilde{F}}{\partial \omega}\right)^2(\delta\omega)^2 + f^2 + \left(\frac{\partial f}{\partial \omega}\right)^2(\delta\omega)^2\right]. \tag{A 4}$$

No cross-product terms are shown since the jitter in the periodic and turbulent motions and the turbulent motions are presumed to be unrelated. When $\tilde{F}$ and f are sinusoidal functions and a top-hat distribution of the frequency jitter is used for simplicity, then

$$\widehat{\left(\frac{\partial \tilde{F}}{\partial \omega}\right)^2} = \widehat{\left(\frac{\tilde{F}}{\omega}\right)^2}, \quad \widehat{\left(\frac{\partial f}{\partial \omega}\right)^2} = \frac{\hat{f}^2}{\omega^2},$$

and the ensemble-averaged variance is

$$\widehat{(\mathscr{F}_j - \hat{F}_j)^2} = \hat{f}^2\left[1 + \left(\frac{(\tilde{F})^2}{\hat{f}^2} + 1\right)\left(\frac{\delta\omega}{\omega}\right)^2\right]. \tag{A 5}$$

Using $(\delta\omega/\omega) \approx 0{\cdot}0015$ from the Gaussian jitter distribution discussed in §2.2 above, then as long as $(\tilde{F})^2/\hat{f}^2 < 4444$ the jitter contributes less than 1 % to the measured ensemble-averaged variance. This indicates that jitter affects turbulence measurements only in the outer region of the boundary layer. No corrections for jitter have been made for the data reported here.

Appendix B. A simple analysis of the effects of probe and wall oscillations on near-wall measurements

One possible source of a measured phase shift in the near-wall region is the oscillation normal to the wall of the measuring sensor relative to the test wall at the imposed unsteadiness frequency. The test wall and/or the measuring sensor may oscillate with respect to the laboratory. For simplicity, let the instantaneous velocity $\mathscr{U}$ be represented by

$$\mathscr{U} = \bar{U}(y) + \tilde{U}_1(y)\cos(\omega t - \phi_u) + u(y, t), \tag{B 1}$$

where $\bar{U}$, $\tilde{U}_1$ and u are the mean, first-harmonic amplitude and turbulent velocities respectively. The instantaneous measuring sensor position with respect to the wall y is given by

$$\hat{y} = \bar{y} + \tilde{y}_1 \cos(\omega t - \phi_y), \tag{B 2}$$

where $\bar{y}$ and $\tilde{y}_1$ are the mean and first-harmonic amplitude for the position. Note that ϕ_u and ϕ_y need not be the same, and when this is the case, as shown below, the *measured* phase angle for the measured velocity can be much different to ϕ_u because of the oscillation of the measuring sensor relative to the test wall.

For purposes of discussion assume that the law-of-the-wall velocity profile holds for quasisteady cases:

$$\hat{U}^+ = \frac{\hat{U}}{\hat{U}_\tau} = f(\hat{y}^+), \tag{B 3}$$

where

$$\hat{U}_\tau = \bar{U}_\tau \left(1 + \frac{\tilde{\tau}_{w1}}{\bar{\tau}_w} \cos(\omega t - \phi_w)\right)^{\frac{1}{2}}, \quad \bar{U}_\tau = \left(\frac{\bar{\tau}_w}{\rho}\right)^{\frac{1}{2}} \tag{B 4}$$

because of the oscillatory surface shearing stress. When the probe oscillates relative to the wall then

$$\hat{y}^+ = \frac{\hat{U}_\tau \hat{y}}{\nu} = \frac{\hat{U}_\tau}{\nu}(\bar{y} + \tilde{y}_1 \cos(\omega t - \phi_y)). \tag{B 5}$$

Using (B 4) and (B 5) in (B 3), the first harmonic of the 'measured' velocity for small $\tilde{y}_1/\bar{y}$ and $A_\tau = \tilde{\tau}_{w1}/\bar{\tau}_w$ values becomes

$$\tilde{U}_m = \bar{U}_\tau [\tfrac{1}{2} A_\tau (f + f' y^+) \cos(\omega t - \phi_w) + \tilde{y}_1^+ f' \cos(\omega t - \phi_y)], \tag{B 6}$$

where $\tilde{y}_1^+ = \tilde{y}_1 \bar{U}_\tau / \nu$. Higher-order terms and turbulent-fluctuation u-contributions to $\tilde{U}_m$ have been neglected. From (B 6) the phase angle of $\tilde{U}_m$ is given by

$$\tan(\phi_m - \phi_w) = \frac{\dfrac{2\tilde{y}_1^+ f'}{A_\tau (f + f' y^+)} \sin(\phi_y - \phi_w)}{1 + \dfrac{2\tilde{y}_1^+ f'}{A_\tau (f + f' y^+)} \cos(\phi_y - \phi_w)}. \tag{B 7}$$

Clearly in this discussion, ϕ_w is the 'true' phase angle when $\tilde{y}_1^+ = 0$. One also will measure this when $\phi_y = \phi_w$, $\phi_y = \phi_w + 180°$, or $f' = 0$.

For the sample calculation presented below

$$f(y^+) = \Delta U^+ + U^+, \tag{B 8}$$

where U^+ is given from the inverse continuous wall law relationship

$$y^+ = U^+ + \frac{\exp(\kappa U^+) - (1 + \kappa U^+ + \frac{1}{2}(\kappa U^+)^2 + \frac{1}{6}(\kappa U^+)^3)}{\exp(\kappa C)} \tag{B 9}$$

with $\kappa = 0{\cdot}41$ and $C = 5{\cdot}1$. The term ΔU^+ is due to the wall-interference effect of hot-wire probes in the viscous sublayer, $y^+ \leqslant 5$, as described by Oka & Kostić (1972) and Hebbar (1980). A good fit to Hebbar'a data is given by

$$A U^+ = \frac{(5 - y^+)^{2{\cdot}66}}{5^{1{\cdot}66}} \quad (y^+ \leqslant 5). \tag{B 10}$$

Figure 30 shows f'/f given by (B 10)–(B 12).

Figure 30 shows $\phi_m - \phi_w$ phase angles that were calculated from (B 7–B 10) for $\tilde{y}_1^+ = 3{\cdot}28$ and for $\tilde{y}_1^+ = 1$ with $A_\tau = \frac{1}{2}$. All curves cross at $y^+ = 2{\cdot}3$ because $f' = 0$ there. Negative values of $\phi_y - \phi_w$ produce negative values of $\phi_m - \phi_w$ beyond this location.

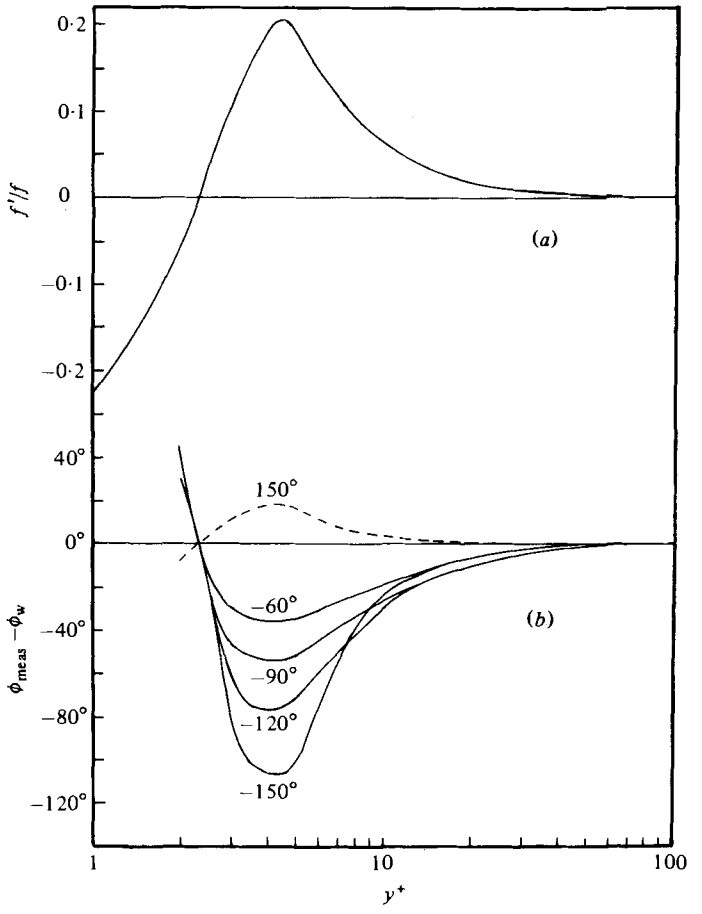

FIGURE 30. (*a*) f'/f *vs.* y^+. (*b*) $(\phi_{\text{meas}}-\phi_{\text{w}})$ *vs.* y^+ for $A_\tau = \frac{1}{2}$; ——, $\tilde{y}_1^+ = 3{\cdot}28$; – – – –, $\tilde{y}_1^+ = 1{\cdot}0$.

Equation (B 7) is an odd function of $\phi_y-\phi_{\text{w}}$. The wall interference effect for $y^+ < 5$ causes $\phi_{\text{m}}-\phi_{\text{w}}$ to be closer to zero than if calculated from (B 9) alone.

Figure 5 shows the experimentally measured phase angles near the wall at 1·34 m where the flow is accelerating. For a large $\tilde{y}_1$ of 0·05 mm, $\tilde{y}_1^+ = 3{\cdot}28$ at this location. The maximum phase lead of about 50° is at $y^+ \approx 14$, rather than at $y^+ = 4{\cdot}5$ as shown in figure 30. The general shapes of these calculated and measured phase-angle curves are the same away from the wall.

Another positive feature of this simple analysis is that it explains why a much larger phase shift is measured in accelerating-flow regions than near separation for a given $\tilde{y}_1$. $\tilde{y}_1^+$ is much larger in regions of flow acceleration than in decelerating flow regions because $\bar{\tau}_{\text{w}}/\rho$ is larger. As experimentally measured, ϕ_{m} is much different from ϕ_{w} near the wall when the flow is accelerating than when near separation.

Some of the difference between the calculated and measured values is no doubt due to the real facts that nearest the wall $\tilde{y}_1/\bar{y}$ is not small and that there is some jitter in the sensor–wall relative position. Furthermore, it was assumed in the calculation that the unsteady-flow hot-wire wall-interference effect was the same as for the steady flow, which is also questionable.

REFERENCES

ACHARYA, M. & REYNOLDS, W. C. 1975 *Thermosciences Div., Dept Mech. Engng, Stanford Univ. Rep.* TF-8.

ASHJAEE, J. & JOHNSTON, J. P. 1980 *Trans. A.S.M.E.* I: *J. Fluids Engng* **102**, 275–282.

BRADSHAW, P. 1978 *AGARD* LS-94, Paper 10.

COLLINS, M. A. & SIMPSON, R. L. 1978 *A.I.A.A. J.* **16**, 291–292.

COUSTEIX, J., DESOPPER, A. & HOUDEVILLE, R. 1977 In *Proc. Symp on Turbulent Shear Flow, Pa. State Univ.*, 18–20 *April*, paper 8-B.

COUSTEIX, J., HOUDEVILLE, R. & RAYNAUD, M. 1979 In *Proc. 2nd Symp on Turbulent Shear Flow, Imperial College, London*, 2–4 *July*, pp. 6.12–6.17.

DAVIS, R. E. 1974 *J. Fluid Mech.* **63**, 673–693.

EATON, J. K., JEANS, A. H., ASHJAEE, J. & JOHNSTON, J. P. 1979 *Trans A.S.M.E.* I: *J. Fluids Engng* **101**, 364–366.

HEBBAR, K. S. 1980 *DISA Info.* no. 25, pp. 15–16.

HOUDEVILLE, R., DESOPPER, A. & COUSTEIX, J. 1976 In *La Recherche Aérospatiale* 1976, pp. 183–191.

KENISON, R. C. 1977 *AGARD* CP-227, Paper 20.

KLINE, S. J., BARDINA, J. G. & STRAWN, R. C. 1981 *AIAA*-81-1220.

KLINE, S. J. & MCCLINTOCK, F. A. 1953 *Mech. Engng* **75**, 3–8.

MILLER, J. A. 1976 *Trans. A.S.M.E.* I: *J. Fluids Engng* **98**, 550–557.

OKA, S. & KOSTIĆ, Z. 1972 *DISA Info.* no. 13, pp. 29–33.

PATEL, M. H. 1977 *Proc. R. Soc. Lond.* A **353**, 121–144.

PERRY, A. E. & SCHOFIELD, W. H. 1973 *Phys. Fluids* **16**, 2068–2074.

PHILLIPS, O. M. 1955 *Proc. Camb. Phil. Soc.* **51**, 220–229.

RUBESIN, M. W., OKUNO, A. F., MATEER, G. G. & BROSH, A. 1975 *NASA Tech. Memo.* X-62, 465.

SCHOFIELD, W. H. 1980 *Australian Defence Sci. & Tech. Org. Aero. Res. Lab. Mech. Engng Rep.* 157 (AR-002-218).

SHILOH, K., SHIVAPRASAD, B. G. & SIMPSON, R. L. 1981 *J. Fluid Mech.* **113**, 75–90.

SHIVAPRASAD, B. G. & SIMPSON, R. L. 1982 *Trans A.S.M.E.* I: *J. Fluids Engng* **104**, 162–166.

SIMPSON, R. L. 1976 *A.I.A.A. J.* **14**, 124–126.

SIMPSON, R. L. 1977 *AGARD* CP-227, Paper 19.

SIMPSON, R. L. 1981 *Trans. A.S.M.E.* I: *J. Fluids Engng* **103**, 520–533.

SIMPSON, R. L. & BARR, P. W. 1975 *Rev. Sci. Instrum.* **46**, 835–837.

SIMPSON, R. L. & CHEW, Y.-T. 1979 In *Proc. 3rd Int. Workshop on Laser Velocimetry*, pp. 179–196. Hemisphere.

SIMPSON, R. L., CHEW, Y.-T. & SHIVAPRASAD, B. G. 1980*a* *Project SQUID Rep.* SMU-4-PU, NTIS AD-A095 252/3.

SIMPSON, R. L., CHEW, Y.-T. & SHIVAPRASAD, B. G. 1980*b* *Dept Civ./Mech. Engng Rep.* WT-6, *Southern Methodist Univ.*, NTIS AD-A090 585/1.

SIMPSON, R. L., CHEW, Y.-T. & SHIVAPRASAD, B. G. 1981*a* *J. Fluid Mech.* **113**, 23–51.

SIMPSON, R. L., CHEW, Y.-T. & SHIVAPRASAD, B. G. 1981*b* *J. Fluid Mech.* **113**, 53–73.

SIMPSON, R. L., HEIZER, K. W. & NASBURG, R. E. 1979 *Trans. A.S.M.E.* I: *J. Fluids Engng* **101**, 381–382.

SIMPSON, R. L., SALLAS, J. J. & NASBURG, R. E. 1978 *Trans. A.S.M.E.* I: *J. Fluids Engng* **100**, 287–290.

SIMPSON, R. L., STRICKLAND, J. H. & BARR, P. W. 1977 *J. Fluid Mech.* **79**, 553–594.

WOOD, N. B. 1975 *J. Fluid Mech.* **67**, 769–786.